NEUROSCIENCE

Egocentric boundary vector tuning of the retrosplenial cortex

Andrew S. Alexander[1,2]*, **Lucas C. Carstensen**[1,2,3], **James R. Hinman**[1†], **Florian Raudies**[1], **G. William Chapman**[1,2], **Michael E. Hasselmo**[1,2,3]

The retrosplenial cortex is reciprocally connected with multiple structures implicated in spatial cognition, and damage to the region itself produces numerous spatial impairments. Here, we sought to characterize spatial correlates of neurons within the region during free exploration in two-dimensional environments. We report that a large percentage of retrosplenial cortex neurons have spatial receptive fields that are active when environmental boundaries are positioned at a specific orientation and distance relative to the animal itself. We demonstrate that this vector-based location signal is encoded in egocentric coordinates, is localized to the dysgranular retrosplenial subregion, is independent of self-motion, and is context invariant. Further, we identify a subpopulation of neurons with this response property that are synchronized with the hippocampal theta oscillation. Accordingly, the current work identifies a robust egocentric spatial code in retrosplenial cortex that can facilitate spatial coordinate system transformations and support the anchoring, generation, and utilization of allocentric representations.

INTRODUCTION

Spatial cognition is a critical component of intelligent behavior. The ability to effectively recall and navigate between known goals relies on stored representations of spatial interrelationships. Further, episodic experiences can be thought of as situated within a stored mental map indicating the places in which events occurred. Spatial representations that support both navigation and episodic memory are observed in many brain regions, including the hippocampus and medial entorhinal cortex, where neurons exhibit receptive fields that are correlated with the position or orientation of the animal relative to the array of locations and cues that define the structure of the outside world. This viewpoint-invariant coordinate system is commonly referred to as the allocentric reference frame (*1*–*3*).

Although it has been repeatedly shown that intact function of allocentric spatial circuits is critical for spatial memory and navigation (*4*, *5*), it is important to consider that all spatial information enters the brain via sensory organs and their corresponding processing streams. Accordingly, knowledge of the position of a prominent landmark and a neighboring goal location would be, at least initially, incorporated into a stored spatial map in egocentric coordinates relative to the animal itself (*6*–*8*). Further, enacting navigational plans can be based on stored allocentric representations but would ultimately require translation into sequences of actions anchored in an egocentric reference frame [e.g., one turns clockwise relative to their own previous orientation position; (*7*–*9*).

Neural mechanisms by which egocentric and allocentric coordinate systems are interrelated are still the subject of intense examination. Computational models have predicted that cortical networks capable of integrating allocentric and egocentric information for either constructing or using stored spatial representations require neurons with egocentric sensitivity to external locations (*7*, *8*). Most investigations into egocentric representations in unconstrained animals have focused on the neural substrates of path integration, a navigational computation wherein self-location is approximated via continuous integration of angular and linear displacement (*10*). Neural correlates of these movement variables have been reported in several structures (*9*, *11*–*14*).

Only recently have externally anchored egocentric representations that extend beyond self-motion been reported (*15*–*20*). Egocentric representations of this nature may anchor to environmental boundaries. Boundaries present a unique intersection between egocentric and allocentric coordinate systems, as they have fixed positions that define the navigable allocentric space and simultaneously restrict the egocentric affordances of the agent such as what can be viewed or what motor plans can be executed. Environmental bounds or walls extend along large regions of an environment and thus enable extended interaction from multiple allocentric or egocentric perspectives. Egocentric neural responses have now been reported in multiple areas such as lateral entorhinal cortex (*19*), dorsal striatum (*16*), and postrhinal cortices (*15*, *17*). However, none of these regions have the reciprocal interconnectivity between egocentric and allocentric spatial circuitry that might mediate bidirectional reference frame transformations.

From a connectivity standpoint, the retrosplenial cortex (RSC) is an excellent candidate to examine egocentric representations during navigation. Further, theoretical work has posited that RSC forms a computational hub for supporting coordinate transformations (*7*, *8*, *21*, *22*). RSC is composed of two interconnected subregions, dysgranular and granular, which have slightly different connectivity with cortical and subcortical regions. Dysgranular RSC (in mice agranular RSC) is positioned along the dorsal surface of the brain and has biased interconnectivity with association, sensory, and motor processing regions that code in egocentric coordinates (*23*, *24*). In contrast, granular RSC has strong reciprocal innervation with the hippocampal formation and associated structures that are primarily sensitive to the allocentric coordinate system (*25*).

---

[1] Center for Systems Neuroscience, Boston University, 610 Commonwealth Ave., Boston, MA 02215, USA. [2] Department of Psychological and Brain Sciences, Boston University, 64 Cummington Mall, Boston, MA 02215, USA. [3] Graduate Program for Neuroscience, Boston University, 610 Commonwealth Ave., Boston, MA 02215, USA.
*Corresponding author. Email: asalexan@gmail.com
†Present address: Department of Psychology, Neuroscience Program, University of Illinois at Urbana-Champaign, Champaign, IL 61820, USA.

Despite having dense reciprocal connectivity with numerous regions known to support spatial cognition, few reports have examined spatial response properties of neurons within the RSC. Most assessments of functional properties of RSC neurons have occurred in rodents performing track running tasks (*26*–*30*). Track running experiments have revealed that RSC neurons exhibit spatial correlates with conjunctive sensitivity to allocentric and egocentric coordinate systems (among others) (*27*). Conjunctive tuning of this type has been shown in modeling work to facilitate spatial coordinate transformations, further supporting a role for RSC in the required transformation between these two spatial reference frames (*7*, *31*). However, grid cells, head direction cells, place cells, and other forms of well-characterized spatial receptive fields have primarily been examined in two-dimensional (2D) environments. Only a few experiments have studied RSC in similar conditions, and all such reports have focused on head direction encoding (*11*, *32*, *33*).

To examine externally referenced egocentric representations in RSC capable of supporting both navigation and reference frame transformations, we recorded from both RSC subregions while rats freely explored familiar 2D environments. We report that subsets of RSC neurons exhibit a variety of spatially stable activation patterns in egocentric and allocentric coordinate systems. These findings support predictions from computational modeling related to translation between spatial reference frames and highlight important navigation-related variables encoded in association cortex (*7*, *8*).

RESULTS

RSC neurons exhibit stable spatial activity during free exploration

We recorded 555 neurons extracellularly in RSC in either hemisphere from male Long-Evans rats ($n = 7$) during free exploration. To enable comparisons between functional properties of neurons recorded in dysgranular versus granular subregions of RSC, we estimated tetrode placement and depth for each session [Fig. 1A ($n = 130$ sessions) and fig. S1, A and B]. Of the total population, 41.5% ($n = 230/555$) were recorded from dysgranular RSC, 15.1% ($n = 84/555$) from the border between dysgranular RSC and granular RSC, and 43.4% ($n = 241/555$) within granular RSC. For baseline sessions, rats foraged for scattered reward in 1.25-m^2 arenas with observable fixed distal cues.

RSC neurons exhibited complex firing rate fluctuations, as rats randomly foraged within open arenas (Fig. 1B). To assess the spatial stability of these representations for each neuron individually, we began by examining correlations between 2D spatial firing ratemaps constructed from first and second halves of each experimental session (Fig. 1C and fig. S2A). Across the full population of RSC neurons, 45.8% of cells ($n = 254/555$) had spatial correlations greater than the 99th percentile ($\rho = 0.23$) of the distribution of correlations observed following 100 random shifts of the complete spike train for each neuron relative to spatial position (Fig. 1C).

In some cases, RSC neurons with spatially anchored responses had slight differences in basic firing properties from those that were not spatially stable (fig. S2B). Of particular interest and consistent with the presence of spatial receptive fields, RSC neurons with spatially reliable activity had significantly more spatial coherence and broader peak firing rate dispersion than nonstable cells (fig. S2, B and C). Spatially anchored firing patterns were also observed at more ventral recording sites, where it was difficult to resolve whether the recording tetrode was in RSC or the cingulum bundle (fig. S2D). Recordings from these sites were not included in the pool of RSC neurons for analysis.

Egocentric boundary vector responsivity of RSC

Of neurons with stable spatial firing in the open field, several had receptive fields that were qualitatively proximal to environmental boundaries (Fig. 1B, right). Inspection of the relationship between each spike and the head direction or movement direction of the animal revealed that these responses manifested when the animal was oriented in a similar manner relative to any wall, suggesting that the receptive field was defined in an egocentric manner. As such, these responses were reminiscent of egocentric boundary cells (EBCs) recently reported in the dorsal striatum (*16*), lateral entorhinal cortex (*19*), and postrhinal cortex (*15*, *17*). To test this explicitly, we constructed egocentric boundary ratemaps (EBRs) using procedures previously described (Fig. 1D) (*16*). Briefly, for each behavioral frame, the distance to the nearest wall in each 3° offset from the animal's head direction or movement direction was calculated (Fig. 1D). The same process is repeated for the position of each spike from each neuron, and then ratemaps in polar coordinates were constructed by dividing the number of spikes by the total behavioral occupancy in seconds.

From each EBR, we computed the mean resultant length (MRL) of angular tuning for the full session as well as the absolute difference in angular tuning direction and distance between first and second halves of the baseline session. RSC cells were determined to exhibit significant egocentric boundary sensitivity if they met the following criteria: (i) they had an MRL for the session that was greater than the 99th percentile of the distribution of resultants computed following repeated shifted spike train randomizations, (ii) they had an absolute difference of mean directional tuning between halves of the baseline session that was less than 45°, and (iii) the change in preferred distance relative to the full session was less than 50% for both halves. Using these metrics, 17.3% ($n = 96/555$) of RSC neurons were determined to be EBCs (Fig. 1, E to G).

Application of a speed threshold (>5 cm/s) modestly increased the MRL and size of the EBC population [Fig. 1H, $n = 106/555$, 19.1%; median MRL difference = 0.006, interquartile range (IQR) = −0.0012 to 0.013; Wilcoxon signed-rank, $z = 4.70$, $P = 2.65 \times 10^{-06}$]. From this result, we hypothesized that egocentric receptive fields of EBCs were defined by the movement direction of the animal rather than head direction, which can be computed even when the animal is motionless. RSC neurons [21.4% ($n = 119/555$)] were determined to be EBCs when referenced to movement direction, but egocentric boundary vectors were overall more strongly tuned to head direction (Fig. 1I, EBC MRL with head direction = 0.22, IQR = 0.17 to 0.29; EBC MRL with movement direction = 0.14, IQR = 0.11 to 0.20, Wilcoxon signed-rank test for zero difference, $z = 9.61$, $P = 7.60 \times 10^{-22}$). A subpopulation of the recorded population, 16.4% ($n = 91/555$), were detected as EBCs when using either head direction or movement direction as the angular reference. However, a subpopulation of neurons were only detected as EBCs when using head direction ($n = 15/555$) or movement direction ($n = 28/555$). Because the directional estimates are largely dependent on one another and there were no differences in the stability of receptive fields for EBCs detected using either (fig. S3, A and B), we pooled these populations (fig. S3B; $n = 134/555$, 24.1%).

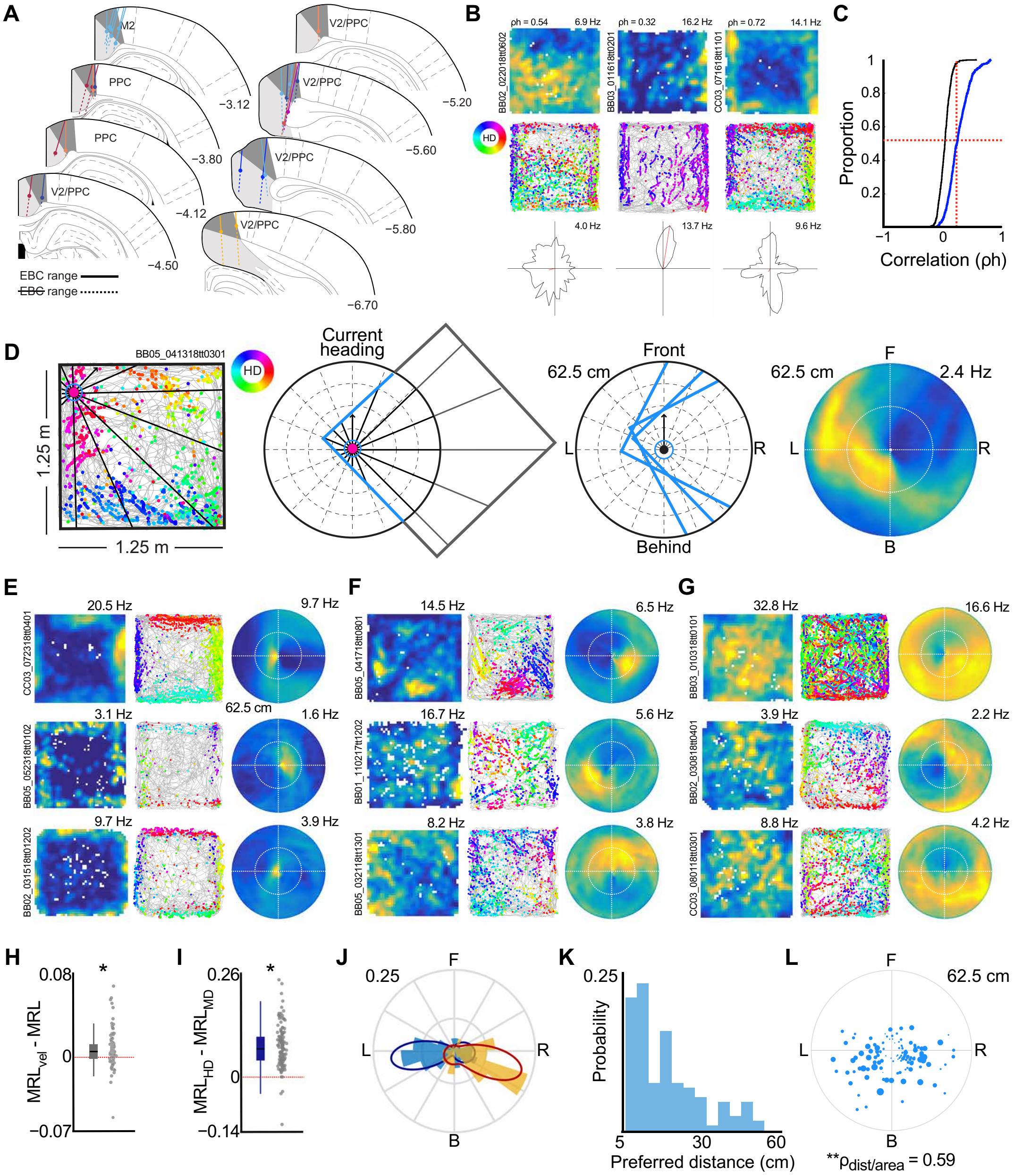

Fig. 1. Egocentric boundary vector representations of RSC neurons during free exploration. (**A**) Locations of RSC tetrode tracts where neurons with egocentric boundary sensitivity were observed. For each tetrode, solid lines indicate range where EBCs were recorded, and filled circles indicate estimation of most ventral location of EBC observation. (**B**) Example 2D ratemaps (top), trajectory plots (middle), and head direction tuning plots (bottom) for three RSC neurons with significant stability in spatial firing. For trajectory plots, the position of the animal throughout the entire experimental session is depicted in gray. The location of individual spikes is shown with colored circles, which indicate the corresponding head direction of the animal according to the legend on the left. (**C**) Cumulative density function depicts Spearman's rho calculated after correlating 2D ratemaps taken from the first and second halves of each experimental session (blue). In black, distribution of spatial stability scores after randomly shifting spike trains relative to position is shown. Red vertical line shows 99th percentile of randomized distribution and its intersection with the real distribution of spatial stability. Percentage of neurons above red horizontal line have significant spatial stability. (**D**) Schematic for construction of EBRs. Left and middle panels: An example spike is mapped with respect to egocentric boundary locations in polar coordinates. Left: The head direction of the animal is determined for each spike (vector with arrow), and the distance to wall intersections for all 360° is determined (subsample shown for clarity). Middle left: Boundaries within 62.5 cm are referenced to the current head direction of the animal for a single spike. Middle right: Example boundary positions for three spikes. Right: Example EBR. (**E**) 2D ratemaps, trajectory plots, and EBRs for three example RSC EBCs with animal-proximal receptive fields. (**F**) Same as in (E) but for three RSC EBCs with animal-distal receptive fields. (**G**) Same as in (E) and (F) but for three RSC EBCs with inverse receptive fields. (**H**) Difference in strength of EBC tuning when a speed threshold was applied (MRL_{vel}) versus no speed threshold (MRL). (**I**) Difference in strength of EBC tuning when egocentric bearing was referenced to head direction (MRL_{HD}) rather than movement direction (MRL_{MD}). (**J**) Polar histogram of preferred orientation of receptive field across all RSC EBCs. Yellow and blue bars correspond to EBCs recorded in the left and right hemisphere, respectively. Overlaid probability density estimates from two-component Von Mises mixture models on distribution of preferred orientation for left (red) and right (blue) hemispheres. (**K**) Distribution of preferred distance of all RSC EBC receptive fields. (**L**) Polar scatter plot of preferred orientation versus preferred distance for the full RSC EBC population. Circle size indicates the area of the egocentric boundary vector receptive field.

Properties of RSC egocentric boundary vector receptive fields

Subpopulations of RSC EBCs exhibited either increased or decreased activation when the animal occupied a particular orientation and distance relative to environmental boundaries (Fig. 1, E to G). In accordance with previous literature, we refer to those neurons that were inhibited as inverse EBCs (Fig. 1G) and neurons with excitatory receptive fields as EBCs (Fig. 1, E and F). Identification of the center of mass of EBC receptive fields (either excitatory or inhibitory) revealed a bimodal distribution of preferred orientations that was best fit by a two-component Von Mises mixture model with means of 108.1° (L) and 249.3° (R) relative to directly in front of the animal (Fig. 1J; number of Von Mises mixture components determined via sequential improvement in log-likelihood ratio and cross-validation, fig. S4). EBCs were recorded in both hemispheres, and there was a contralateral relationship between the preferred orientation and the hemisphere in which the neuron was recorded, with larger numbers of rightward EBC receptive fields recorded in the left hemisphere and vice versa (Fig. 1J, right-hemi EBCs preferring left side = 32/54, 59.3%; left-hemi EBCs preferring right side = 55/80, 68.8%; Watson-Williams test, $F = 41.93$, $P = 1.7 \times 10^{-9}$). The distribution of preferred distances was skewed toward animal-proximal receptive fields, with numerous EBCs having receptive fields extending beyond range of direct somatosensory stimulation of whiskers (Fig. 1K). Further, the size of EBC receptive fields increased as a function of the preferred distance of the egocentric vector, indicating that the resolution of the representation was dependent on proximity to boundaries (Fig. 1L, Spearman's $\rho = 0.59$, $P = 5.1 \times 10^{-14}$). The presence of EBCs with preferred distances distal to the animal suggested that the EBC response property was not dependent on physical interaction with arena borders.

EBC responses are localized within dysgranular RSC but lack topographic organization

Egocentric boundary vector sensitivity was primarily observed in dysgranular RSC, where 38.7% (n = 89/230) of neurons recorded were classified as EBCs (fig. S1C). In contrast, EBCs were observed in 9.9% (n = 24/241) of granular RSC and 25.0% (n = 21/84) of intermediary area cells between the two subregions. By and large, the distribution of EBCs among RSC subregions was consistent across animals (fig. S1C). The EBC response property was observed across a wide range of anterior/posterior (A/P) coordinates spanning most of the RSC but had no further anatomical organization beyond subregion specificity (range = 2.9 to 6.8 mm relative to bregma, fig. S1D). The distribution of spike waveform widths across all RSC neurons was bimodal, with identified EBCs primarily found in the cluster of neurons with longer duration waveforms (fig. S1E, k-means clustering on waveform width, cluster 1 median = 0.15 s, IQR = 0.15 to 0.18 s, EBCs in cluster 1, n = 9/175, 5.1%; cluster 2 median = 0.31 s, IQR = 0.31 to 0.34 s; EBCs in cluster 2, n = 125/380, 32.9%). Further, EBCs had overall low mean firing rates (fig. S1E, EBCs = 1.62 Hz, IQR = 0.90 to 2.75 Hz, not-EBCs = 3.58 Hz, IQR = 1.15 to 8.51 Hz). Together, the EBC subpopulation was determined to be primarily composed of putative principal neurons, suggesting that the EBC signal is propagated across RSC subregions or into other brain regions.

EBCs could often be simultaneously recorded, which enabled an analysis of potential topography in the distribution of preferred distance and orientation of the egocentric boundary vector. Overall, 142 pairs of RSC EBCs were co-recorded across 29 sessions. Of these pairs, 31.7% (n = 45/142) were recorded on the same tetrode (fig. S5A), while the remaining 68.3% of EBC pairs (n = 97/142) were concurrently recorded on different tetrodes (fig. S5B).

To assess whether there was organization to preferred orientation and distance as a function of proximity of two EBCs (i.e., observed on the same or different tetrodes), we next calculated the difference in receptive field center of mass for both angular and distance components for all pairs. Neither preferred distance nor orientation was statistically different for EBCs recorded on the same versus different tetrodes (fig. S5, C and D, absolute difference in preferred distance same tetrode = 7.5 cm, IQR = 5 to 12.5 cm; absolute difference in preferred distance different tetrode = 10 cm, IQR = 2.5 to 17.5 cm; Wilcoxon rank sum test, $z = -1.44$, $P = 0.15$; absolute difference in preferred orientation same tetrode = 63°, IQR = 20.25 to 93°; different tetrodes = 66.0°, IQR = 24.0 to 114.1°; Wilcoxon rank sum test, $z = -1.08$, $P = 0.28$). Accordingly, we conclude that there is a lack of topographic organization of egocentric boundary vector tuning in the RSC.

Egocentric boundary vector tuning in secondary motor cortex and posterior parietal cortex but not medial entorhinal cortex

In three animals, a subset of more anterior recording tetrodes were positioned in secondary motor cortex [M2, from bregma: A/P: −1.1 to −2.9 mm, medial/lateral (M/L): ±0.8 to 1.2 mm], and 56 neurons were recorded there (fig. S6A). Of M2 neurons, 37.5% reached EBC criterion (n = 21/56, fig. S6B). Similarly, 95 neurons across five rats were recorded in posterior parietal cortex (from bregma: A/P: −3.7 to −5.9 mm, M/L: ±1.5 to 2.4 mm) and a subpopulation of 21.1% (n = 20/95) reached EBC criterion (fig. S6, C and D). EBCs and inverse EBCs were observed in both structures, and receptive fields had similar angular and distance distributions as those observed in RSC (fig. S6, E and F). In contrast, only 3.0% (n = 9/297) of medial entorhinal cortex neurons recorded in similar conditions reached EBC criterion, indicating that the egocentric vector signal was generally not present within the region (fig. S6H) (*19*).

EBC responsivity is not explained by self-motion correlates

In free exploration, spatial locations near environment boundaries uniquely restrict the behavioral affordances of the animal. Many observed EBC receptive fields were proximal to the rat, firing only when the animal was close to boundaries and thus most limited in its possible actions. We next tested whether the manifestation of egocentrically referenced boundary vector tuning was in actuality reflective of self-motion–related firing that was stereotyped near borders.

We began by constructing self-motion–referenced firing ratemaps during open-field sessions (*9*, *32*). The angular difference between movement direction ($\Delta\theta$) and the Euclidian distance in 2D location (Δd) was calculated across a sliding 100-ms window for every position of the animal throughout a free exploration session (Fig. 2A, left). These displacement values were converted to Cartesian coordinates referenced to the previous location of the animal at each step, thus producing a map of the distance and direction of movement of the animal for all position samples within the exploration session (Fig. 2A, middle and right).

Firing rate as a function of these displacement values is presented for representative RSC neurons in Fig. 2 (C to F). The zero-line intersection indicates the position of the animal at the beginning of each 100-ms window, and the x and y axes reflect displacement in lateral and longitudinal dimensions, respectively. Thus, values to the right of

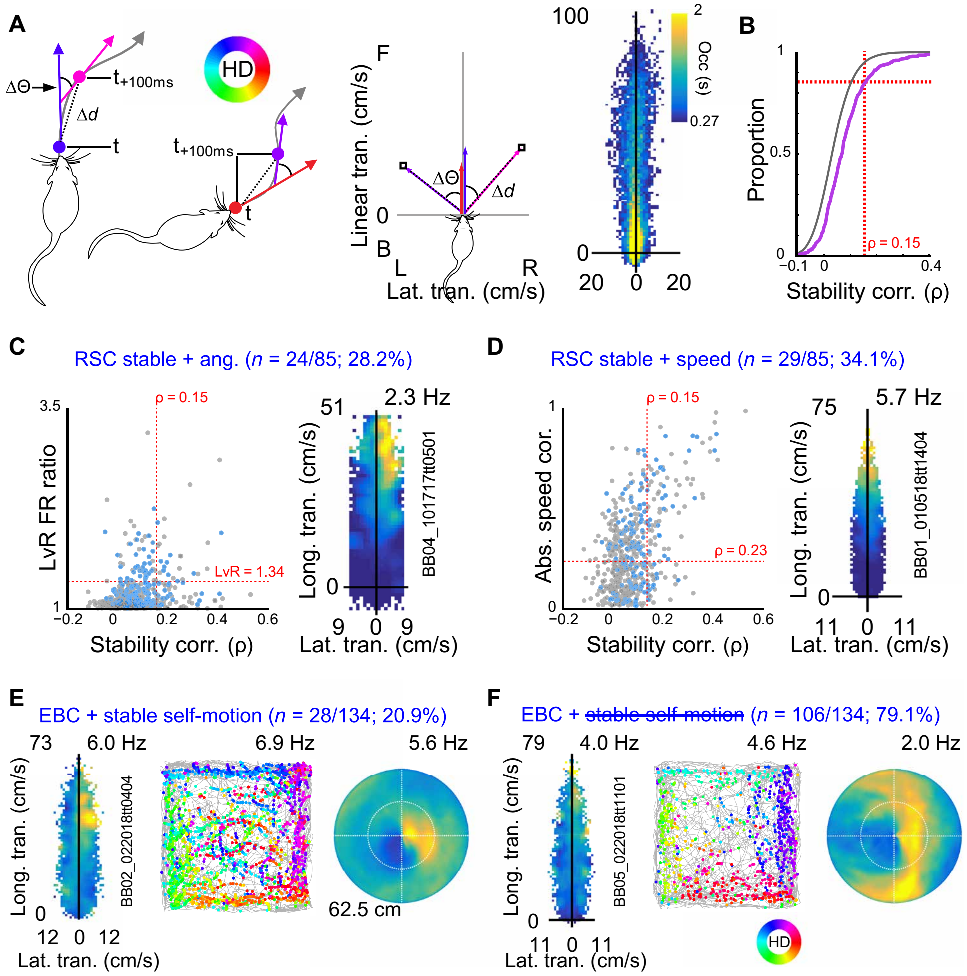

Fig. 2. RSC egocentric boundary vector representations cannot be explained purely by self-motion correlates. (**A**) Schematic of generation of self-motion referenced ratemaps. Left: Example angular and distance translation across 100-ms temporal windows for two hypothetical position samples. Middle: Corresponding lateral and longitudinal translation for left examples in self-motion referenced coordinates. Right: Heat map depicting mean occupancy in seconds for lateral and longitudinal translation combinations across a complete experimental session. Δ*d*, distance displacement; Δθ, angular displacement; colored arrows depict individual position samples 100 ms apart; gray arrow, hypothetical trajectory. (**B**) In pink, cumulative density functions for self-motion ratemap stability values (Spearman's ρ) for all RSC neurons (randomization in gray). Red vertical line shows 95th percentile of randomized distribution and its intersection with the real distribution of spatial stability. Percentage of neurons above red horizontal line have significant self-motion stability. (**C**) Left: Self-motion stability score (*x* axis) versus absolute ratio of activity on left versus right halves of self-motion ratemaps (*y* axis) for all RSC neurons. Blue dots correspond to identified RSC EBCs. Red lines and corresponding values correspond to 95th percentiles of randomized distributions for both metrics. Neurons with values in upper right region were determined to have significant angular displacement tuning. Right: Example RSC neuron with significant firing rate modulation for clockwise movements. (**D**) On the left, same as in (C) but for self-motion stability score versus absolute correlation between mean firing rate and longitudinal displacement ("speed"). Right: Example RSC neuron with significant firing rate modulation as a function of longitudinal displacement. (**E**) Example RSC EBC with stable self-motion correlates. (**F**) Example RSC EBC without stable self-motion correlates.

the vertical zero line reflect the activity of the neuron when the animal moved to the right relative to the previous position and direction of its body axis, and the distance that the action took the animal is reflected in the position of the value along the *y* axis.

To quantify the stability of self-motion tuning, we correlated self-motion ratemaps for each neuron that were individually computed from interleaved temporal epochs (1 s in duration) within the free exploration session. A subset of RSC neurons [15.3% ($n = 85/555$)] exhibited self-motion–related activity that had greater stability than the 95th percentile of the distribution of stability correlation values calculated following permutation tests (Fig. 2B). Of this subpopulation, 28.2% ($n = 24/85$) had firing rate modulation that was biased for leftward or rightward movements (Fig. 2C), while 34.1% ($n = 29/85$) were sensitive to longitudinal movements consistent with speed tuning (Fig. 2D). Of the EBC population, 20.9% ($n = 28/134$) met the stability criteria, indicating that a small subpopulation of neurons exhibiting egocentric boundary vector tuning had stable self-motion correlates (Fig. 2E). However, the vast majority of RSC EBCs did not exhibit self-motion correlates, confirming that egocentric boundary vector tuning was primarily not an epiphenomenon of movement-related activity near borders (Fig. 2F, $n = 106/134$, 79.1%).

Beyond EBCs, the present analysis demonstrated overall limited self-motion tuning in RSC during free exploration. This observation shines new light on previously reported turn-sensitive neurons in RSC during track running tasks (*27*). In previous work, the magnitude of clockwise or counterclockwise activation during track running was demonstrated to be generally insensitive to the magnitude of angular velocity on a trial-by-trial basis. In combination with the lack of self-motion tuning during free foraging observed here, the results collectively suggest that reported egocentric correlates in RSC are externally referenced and unrelated to the speed of angular movement.

Generalized linear models demonstrate robust egocentric vector tuning of RSC EBCs

Self-motion is necessarily conflated with egocentric boundary vector tuning because the response primarily manifested during movement. An EBC may exhibit stable firing rate fluctuations as a function of self-motion that are driven by the egocentric boundary vector receptive field, not the action state of the animal. For example, an EBC with a receptive field to the animal's left may also show self-motion tuning for clockwise movements as a result of the animal being more likely to turn clockwise when there is a wall occupying the egocentric receptive field. Yet, the same neuron may not be activated when the animal turns clockwise in other locations within the environment that do not satisfy the egocentric boundary vector. Thus, although informative about the prevalence of self-motion sensitivity in RSC, a different approach was required to tease out the influence of self-motion and other potential spatial covariates on EBC activity patterns.

We next implemented a generalized linear model (GLM) framework to predict the probability of spiking at each time point as a function of the relative influence of classes of allocentric, self-motion, or EBC-related predictors (Fig. 3A). Allocentric predictors included the head direction of the animal and x and y positions within the arena. Self-motion–related predictors included linear speed and angular displacement (i.e., the differential of animal movement direction in 100-ms windows).

EBC-related predictors were more complicated as a single position sample or spike had relationships to multiple locations along boundaries simultaneously. Accordingly, the EBC predictor could take many forms. To minimize the number of subpredictors, EBC predictors were composed of the animal's distance and egocentric bearing to the center of the arena. Unlike arena boundaries, the center of the arena is a single coordinate that can be described as a function of individual angular and distance components or their conjunction for each position sample (fig. S7A). Critically, EBCs were found to exhibit robust egocentric bearing and distance tuning to the center of the arena, making the predictor a reasonable counterpart to referencing single unit activity to arena walls (fig. S7, B to D).

We assessed the overall influence of each predictor class (allocentric, self-motion, and EBC-related) on model fit by constructing a nested GLM, dropping each predictor class, and then making comparisons between resulting model fits. Figure 3B depicts the difference of Akaike information criteria (dAIC), a metric of the decrement to model fit, for both EBCs and non-EBCs between the full model and reduced models, with all allocentric, self-motion, or egocentric boundary predictors removed. Larger dAIC values indicate greater impact of the predictor class within the full model. Models without EBC and allocentric predictors had significant differences in fit between EBCs and non-EBCs (Fig. 3B, Kruskal-Wallis, $\chi^2 = 270.73$, $P = 1.95 \times 10^{-56}$, post hoc Scheffe test EBC predictors, $P = 1.73 \times 10^{-39,}$ post hoc Scheffe test allocentric predictors, $P = 0.03$). There was no difference between these subpopulations of RSC neurons for the removal of self-motion covariates from the model, further supporting that EBCs were not more sensitive to speed or angular displacement than the remainder of the RSC population (Fig. 3B, post hoc Scheffe test self-motion predictors, $P = 0.17$).

A clear divergence emerged in the importance of EBC-related predictors for the EBC and non-EBC subpopulations. As reflected in the difference in magnitude of dAIC, EBC predictors had greater impact than either allocentric or self-motion predictors for the EBC population (Fig. 3C, blue; dAIC_{EBC}-$\text{dAIC}_{\text{Allo}}$ for EBCs = 186.8, IQR = 33.8 to 450.9; dAIC_{EBC}-dAIC_{SM} for EBCs = 238.8, IQR = 44.1 to 507.1) in contrast to the non-EBC population, which had similar dAIC scores (near 0) for models lacking EBC predictors and other predictor classes (Fig. 3C, gray; dAIC_{EBC}-$\text{dAIC}_{\text{Allo}}$ for non-EBCs = −15.3, IQR = −113.3 to 9.8; dAIC_{EBC}-dAIC_{SM} for non-EBCs = −0.05, IQR = −22.5 to 29.8). Overall, the impact of EBC-related predictors relative to other predictor classes was significantly greater for EBC versus non-EBC subpopulations (dAIC_{EBC}-$\text{dAIC}_{\text{Allo}}$ for EBCs versus non-EBCs, Wilcoxon rank sum, $z = 12.0$, $P = 1.68 \times 10^{-33}$; dAIC_{EBC}-dAIC_{SM} for EBCs versus non-EBCs, Wilcoxon rank sum, $z = 11.2$, $P = 2.60 \times 10^{-29}$). EBCs observed in both parietal cortex and M2 were also substantially more influenced by egocentric vector predictors than either allocentric or self-motion predictor classes (fig. S6G; parietal cortex: dAIC_{EBC}-$\text{dAIC}_{\text{Allo}}$ for EBCs versus non-EBCs, Wilcoxon rank sum, $z = 3.01$, $P = 0.003$; dAIC_{EBC}-dAIC_{SM} for EBCs versus non-EBCs, Wilcoxon rank sum, $z = 4.55$, $P = 5.35 \times 10^{-6}$; M2: dAIC_{EBC}-$\text{dAIC}_{\text{Allo}}$ for EBCs versus non-EBCs, Wilcoxon rank sum, $z = 3.72$, $P = 1.96 \times 10^{-4}$; dAIC_{EBC}-dAIC_{SM} for EBCs versus non-EBCs, Wilcoxon rank sum, $z = 3.42$, $P = 6.29 \times 10^{-4}$).

These results suggested that although models without allocentric or self-motion predictors could yield significantly decreased model fit, the vast majority of EBC neurons were significantly more affected by EBC predictors. Two example EBCs in Fig. 3D illustrate this point, wherein a spike train generated from the output of each model was used to construct trajectory plots and EBRs. In both cases, the model lacking egocentric orientation and distance information yields a trajectory plot and EBR that is substantially poorer at reconstructing the actual data than any other reduced model.

Although egocentric predictors were the dominant influence on EBC activation, all EBCs were statistically affected by the removal of more than one predictor category (assessed via chi-square tests of log-likelihood ratios, $P < 0.001$). In this manner, the GLM analyses also revealed that RSC EBCs were conjunctively sensitive to the position of arena boundaries in egocentric coordinates and allocentric heading or location simultaneously. This feature of EBC responsivity is consistent with theoretical work proposing a transformation between egocentric and allocentric spatial representations within RSC (*7*).

GLM confirms vectorial representation

The use of the GLM framework provided an opportunity to verify that RSC neurons with egocentric boundary sensitivity actually formed vector representations of the relationships between environmental boundaries and the animal. By dropping out egocentric bearing and egocentric distance from the model individually, we were able to investigate the relative influence of the individual components of the egocentric boundary vector in isolation for each neuron.

Significant model decrements were observed in 93.3% (n = 125/134) of EBCs following removal of the egocentric bearing component and 55.9% (75/134) of EBCs were affected by the removal of egocentric distance predictors. Overall, the magnitude of error to model fit was substantially greater when egocentric bearing was removed,

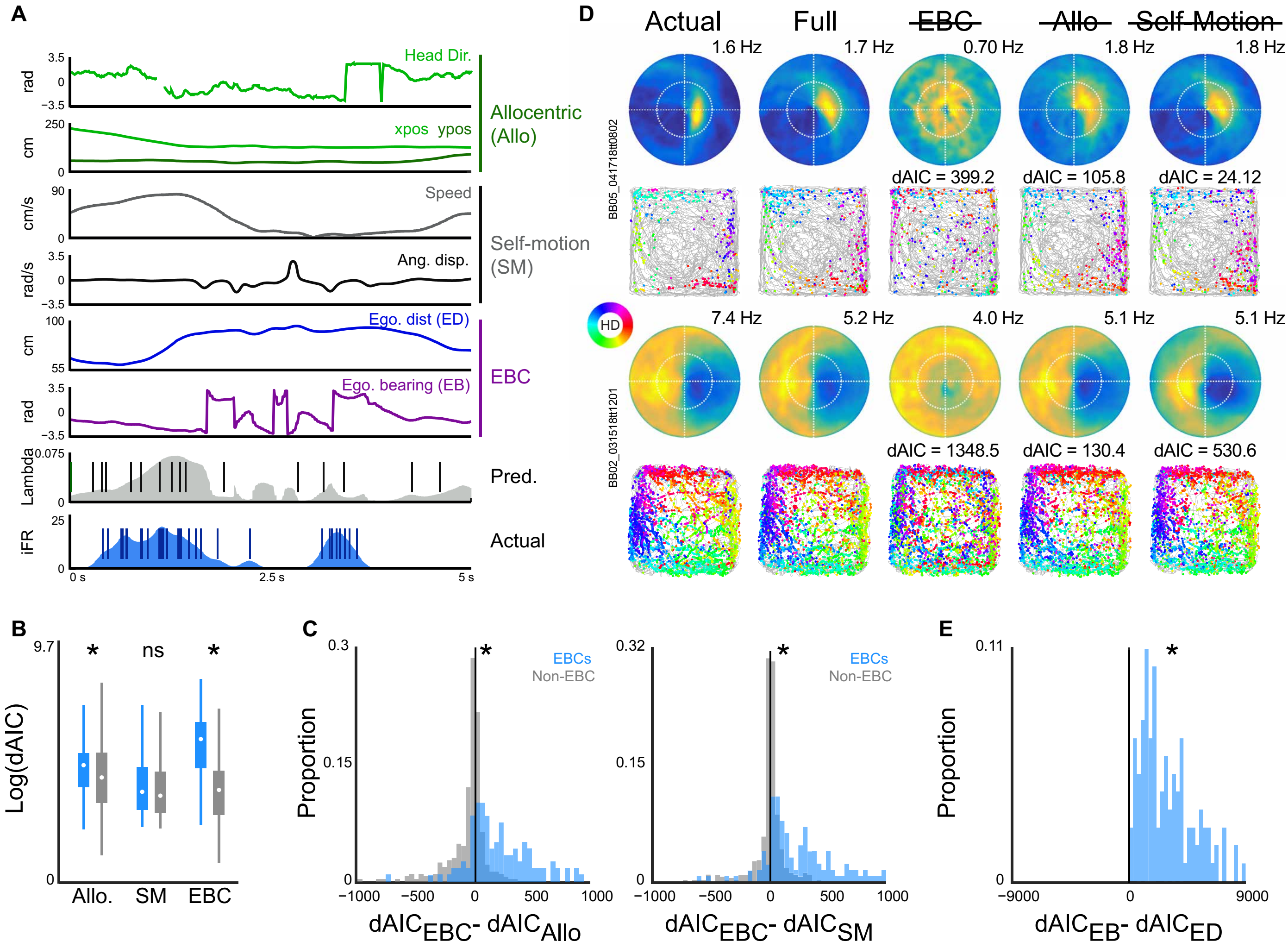

Fig. 3. Egocentric vector tuning is more robust than allocentric or self-motion correlates using a generalized linear modeling framework. (**A**) Example GLM predictors composing allocentric, self-motion, and egocentric vector classes with corresponding actual and predicted firing rates and spike trains over a 5-s window. (**B**) Boxplots depicting median and quartiles of log-transformed dAIC scores for models, with all allocentric, self-motion, or egocentric vector predictors removed (blue bars, EBCs; gray bars, non-EBCs). Larger dAICs indicate greater error in model fit with removal of a predictor class. (**C**) Comparison of dAIC scores for models with egocentric vector versus allocentric predictors removed (left) or egocentric vector versus self-motion predictors removed (right) for EBCs (blue) and non-EBCs (gray). Rightward shifts indicate greater error in model fit for models with removed egocentric vector predictors. (**D**) For two example RSC EBCs, predicted GLM spike trains from all models were used to construct EBRs and trajectory plots. Left column: Actual EBR and corresponding trajectory plot below. Second column: For the same cell, an EBR and corresponding trajectory plot for the GLM constructed using all egocentric vector, allocentric, and self-motion predictors. Final three columns: EBRs and trajectory plots for each reduced model and corresponding dAIC scores. (**E**) Comparison of dAIC scores for models with the egocentric bearing versus the egocentric distance removed reveal greater impact of egocentric bearing for EBCs.

indicating that, although both distance and orientation components are critical for egocentric boundary vector responsiveness, the directional component more robustly drives neurons exhibiting this tuning preference (Fig. 3E, difference in dAIC for egocentric bearing versus egocentric distance = 2269.7, IQR = 1283.3 to 3767.5; Wilcoxon signed-rank test, $z = 9.7$, $P = 2.96 \times 10^{-22}$).

Consistent with observations from the GLM, the number of detected EBCs decreased as the allowed variability in preferred distance across the session was systematically decreased (fig. S8, i.e., detected EBCs were required to have more reliable distance tuning across the session). These results indicate that although a large proportion of RSC neurons can be described as having egocentric boundary vectors, a number of neurons are primarily responsive to egocentric boundary bearing as observed in the lateral entorhinal and postrhinal cortices (*15*, *17*, *19*).

EBCs respond to local, not distal, environmental features

Characterization of EBC properties and self-motion correlates were conducted in baseline sessions in which the open arena remained in a fixed location relative to the experimental room and fixed distal cues therein. We next conducted a series of experimental manipulations of the relationship between the familiar arena and the testing room to confirm that EBC response properties were defined by the relationships between environmental boundaries and the animal itself.

First, we rotated the open field 45° to maximally disrupt correspondence between arena and distal walls or cues present within the recording environment to verify that EBC responses were anchored to local boundaries and not the broader recording room. Under these conditions, we recorded a total of 65 RSC neurons (across four rats and 14 sessions), of which 44.6% (n = 29/65) had EBC sensitivity. Consistent with EBC responses being referenced to the rat, receptive fields in rotated arenas maintained the same orientation and distance with respect to the animal, although arena boundaries now fell along completely different allocentric axes (Fig. 4, A to C; difference between baseline and rotated preferred orientation = 9°, IQR = −11.25 to 33.0°; Wilcoxon signed-rank test, z = 1.17, P = 0.24;

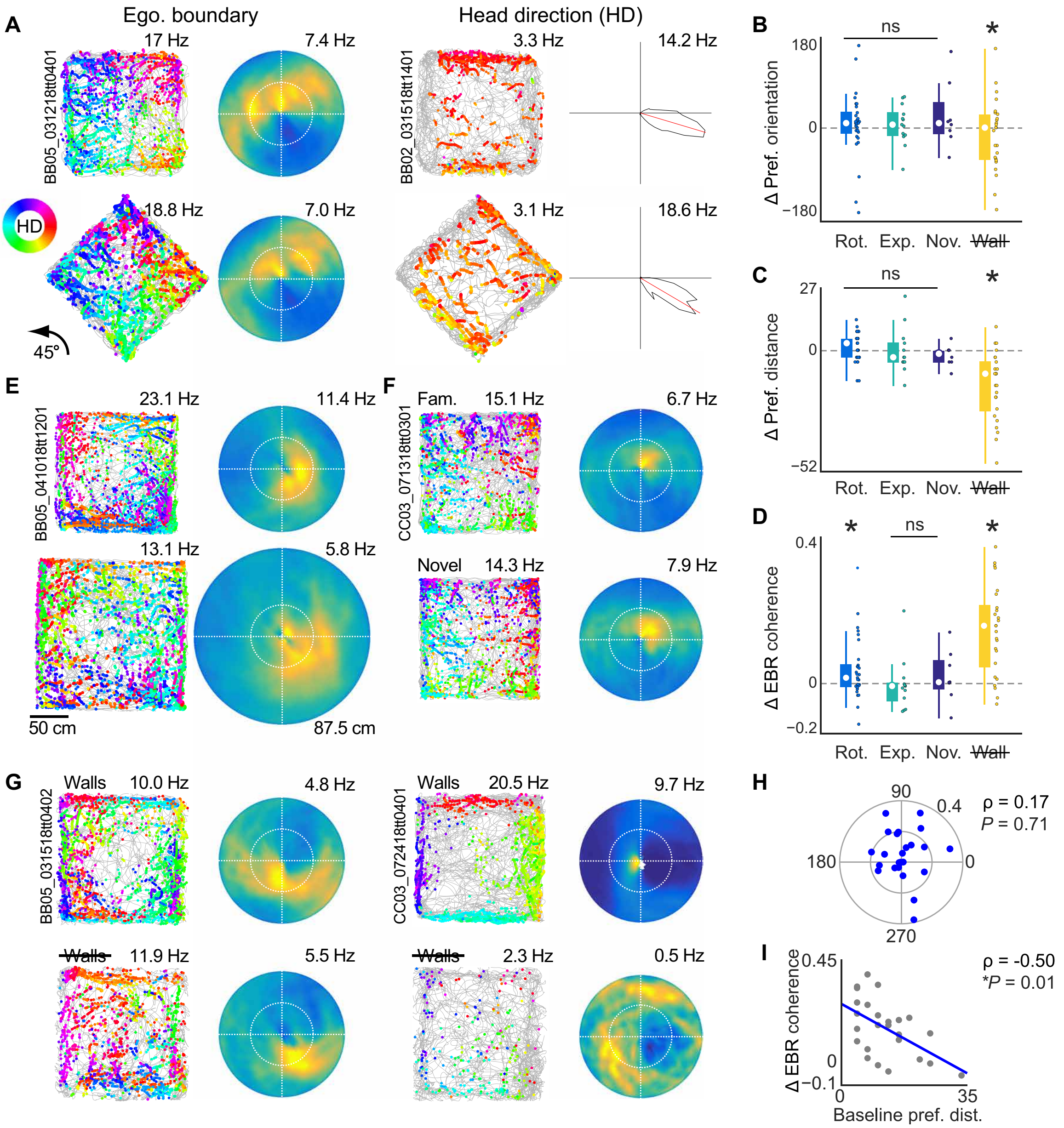

Fig. 4. EBCs are anchored to local boundaries, respond in novel environments, and lose sensitivity in arenas without explicit borders. (**A**) Left: Trajectory plot and EBR for an example EBC with similar egocentric boundary vector tuning in baseline experimental session (top) and a second session in an environment rotated 45° (bottom). Right: Example head direction neuron sustains directional tuning across both conditions. (**B**) Preferred orientation of EBC receptive fields in all arena manipulation sessions subtracted from the preferred orientation in baseline sessions. (**C**) Preferred distance of EBC receptive fields in all arena manipulation sessions subtracted from the preferred distance in baseline sessions. (**D**) EBC receptive field coherence in all arena manipulation sessions subtracted from receptive field coherence in baseline sessions. (**E**) Trajectory plot and EBR for an example EBC with similar egocentric boundary vector tuning in baseline experimental session (top) and a second session in an expanded arena (bottom). (**F**) Trajectory plot and EBR for an example EBC with similar egocentric boundary vector tuning in baseline experimental session (top) and a second session in a novel arena (bottom). (**G**) Trajectory plot and EBR for two example EBCs between baseline session (top) and session with walls removed (bottom). Left EBC has a more distal receptive field and exhibits similar egocentric boundary vector tuning. Right EBC has a more proximal receptive field and has disrupted tuning in arena with no walls. (**H**) For EBCs recorded in arenas without walls, the preferred orientation at baseline plotted against the change in EBC receptive field coherence between the two sessions is shown. (**I**) Same as (H) but for change in coherence as a function of baseline preferred distance.

difference between baseline and rotated preferred distance = 3.0 cm, IQR = −3.0 to 5 cm; Wilcoxon signed-rank test, z = 1.44, P = 0.15). Although vector tuning remained intact, there were slight but significant changes to ratemap coherence between baseline and rotation sessions, which suggested that the quality of the egocentric boundary receptive field was decremented across conditions (Fig. 4D; difference between baseline and rotated ratemap coherence = 0.02, IQR = −0.01 to 0.04; Wilcoxon signed-rank test, z = 2.12, P = 0.03).

Consistency in tuning could emerge if the allocentric map anchored to local boundaries rather than distal cues. This was not the case, as a population of simultaneously recorded head direction cells (n = 4; Fig. 4A, right) exhibited similar mean tuning across the rotated and nonrotated conditions (n = absolute median tuning difference = 11.9°, absolute maximum tuning difference = 20.9°). Accordingly, arena rotation experiments dissociated the directional component of EBCs from the allocentric reference frame of head direction cells.

EBC responsivity is anchored to boundaries, not the center of the environment

RSC EBCs exhibited egocentric vector sensitivity to both arena boundaries and the center of the environment, which we used to our advantage in GLM analyses (fig. S7). This occurs because arena boundaries have a fixed relationship relative to the center of the environment. Accordingly, an obvious question is whether the egocentric boundary response is in actuality defined as an egocentric vector to the center of the arena. We addressed this possibility by comparing preferred orientation and distance for 13 RSC EBCs (from four rats across 11 sessions) between baseline arenas and open fields expanded up to 1.75 m^2 (Fig. 4E).

If EBC responses were anchored to boundaries, we anticipated that the orientation and preferred distance would remain consistent across both conditions. Conversely, if the receptive field was defined by a vector to the center of the arena, then the distance component of the egocentric boundary vector would remain fixed to this point. In this scenario, the preferred distance would either move away from the animal in expanded arenas or potentially scale with the arena expansion. We observed that the preferred orientation, preferred distance, and ratemap coherence were not altered between baseline and expanded field sessions, confirming that EBCs were anchored to boundaries and not the center of the arena (Fig. 4, B to D, difference between baseline and expanded preferred orientation = 6°, IQR = −15.75 to 32.25°; Wilcoxon signed-rank test, signed-rank = 55.5, P = 0.51; difference between baseline and expanded preferred distance = −3 cm, IQR = −5.0 to 3.5 cm; Wilcoxon signed-rank test, signed-rank = 30, P = 0.51; difference between baseline and rotated ratemap coherence = −0.01, IQR = −0.04 to 0.01; Wilcoxon signed-rank test, signed-rank = 31, P = 0.34).

EBC responsivity is stable in novel environments

Neurons within the broader neural spatial circuitry such as grid cells, head direction cells, and place cells exhibit consistent, albeit remapped, spatial receptive fields in novel environments. We next questioned whether egocentric boundary vector–tuned neurons of RSC would exhibit similar stability in their selectivity. We recorded 17 RSC cells including 8 EBCs in familiar then novel environment sessions (Fig. 4F, four rats across five sessions). Neither distance nor orientation components of the egocentric boundary vector were altered in the novel environment relative to baseline, illustrating that EBCs are not experience dependent and do not remap between environments (Fig. 4, B and C, difference between baseline and novel preferred orientation = 9°, IQR = −12 to 52.5°; Wilcoxon signed-rank test, signed-rank = 23.5, P = 0.48; difference between baseline and novel preferred distance = −1.5 cm, IQR = −5 to 0 cm; Wilcoxon signed-rank test, signed-rank = 3, P = 0.31). Coherence of EBC receptive fields was unchanged between environments, providing evidence that the resolution of the egocentric location signal was robust in both familiar and novel arenas (Fig. 4D; difference between baseline and novel ratemap coherence = 0.01, IQR = −0.02 to 0.06; Wilcoxon signed-rank test, signed-rank = 22, P = 0.64).

Stability of EBC subpopulations requires physical boundaries

Sensory information originating from multiple modalities likely underlies the egocentric nature of the RSC boundary vector responses. There are two reasons to believe that somatosensation may inform the preferred orientation and distance of a subset of EBCs. First, many RSC neurons with egocentric boundary vector tuning had preferred distances that were proximal to the animal and within or near whisker range (the preferred distance was less than 10 cm for a subset of 24.7% of EBCs; Fig. 1K). Second, the preferred orientation of EBCs spanned all egocentric bearing angles but was biased laterally (in a contralateral manner), perhaps reflecting whisker interaction with borders (Fig. 1J). As such, we questioned whether the presence of a physical boundary was required for EBC spatial tuning and/or particular subsets of EBC receptive fields.

To this end, baseline sessions were compared to recordings in environments that were bordered by drop-offs with no arena walls (n = 35 neurons from seven sessions across three rats). Twenty-five neurons recorded under these conditions exhibited EBC sensitivity in the baseline session (Fig. 4G). EBCs detected in the baseline session had similar preferred orientations but more distal preferred distances in sessions with no physical walls (Fig. 4, B and C, difference between baseline and no walls preferred orientation = 0°, IQR = −63.75 to 27.75°; Wilcoxon signed-rank test, z = −1.02, P = 0.31; difference between baseline and no walls preferred distance = −10.0 cm, IQR = −25.75 to −4.5 cm; Wilcoxon signed-rank test, z = −3.86, P = 1.12×10^{-4}). In addition, the overall coherence of the egocentric receptive field was significantly decreased in the absence of physical walls and fewer EBCs were detected in these sessions (Fig. 4D; difference between baseline and no walls ratemap coherence = 0.16, IQR = 0.05 to 0.22; Wilcoxon signed-rank test, z = 3.94, P = 8.1×10^{-5}; EBCs with no walls = 48.6%, n = 17/35; EBCs with walls = 68.6%, n = 24/35). Collectively, these results suggest that the EBC population signal is degraded in the absence of explicit borders.

Despite this fact, numerous EBCs sustained their preferred egocentric vector across conditions. To investigate why some neurons were disrupted and not others, we next examined the difference in receptive field coherence as a function of baseline preferred orientation and distance. There was no relationship between the baseline preferred orientation of the neuron and the magnitude of degradation of the spatial signal with no physical walls (Fig. 4H, circular-linear correlation, ρ = 0.17, P = 0.71). In contrast, the more proximal the egocentric boundary receptive field was to the animal at baseline, the more decreased the tuning was in an arena with no physical walls (Fig. 4I, Spearman's correlation, ρ = −0.50, P = 0.01). These results support the idea that the subset of animal-proximal EBCs (Fig. 1E) may rely on somatosensory interaction with borders, while EBCs with more animal-distal receptive fields (Fig. 1F) are preserved in environments with no physical walls because they rely on other sensory modalities.

RSC EBCs are insensitive to environmental geometry, which yields a directional representation of environment shape

Boundaries are unique environmental features in that they both restrict navigational affordances and define the spatial structure of the broader environment. Accordingly, the presence of boundary-sensitive neurons within RSC indicates that the region is capable of detecting features of environmental geometry. In a square open field like the one used for baseline experimental sessions, there are two primary defining features of environmental geometry: (i) conjunctions of walls forming 90° corners and (ii) boundaries that are orientated along two axes of allocentric environmental directions. As such, we questioned whether EBCs would maintain their preferred tuning in circular environments that excluded both of these geometric features.

We recorded 23 RSC EBCs as animals free foraged in square and circular environments across two experimental sessions each day (Fig. 5A, total RSC neurons recorded under these conditions = 32 across four rats and 10 sessions). As with most other environmental manipulations, EBC boundary vectors were unchanged when the geometry of the environment was altered (Fig. 5B, difference between square and circle preferred orientation = −9.0°, IQR = −28.5 to 15.75°; Wilcoxon signed-rank test, $z = -1.14$, $P = 0.25$; difference between square and circle preferred distance = −3.0 cm, IQR = −8.0 to 2.75 cm; Wilcoxon signed-rank test, $z = -1.60$, $P = 0.11$; difference between square and circle ratemap coherence = −0.01, IQR = −0.03 to 0.03; Wilcoxon signed-rank test, $z = -0.76$, $P = 0.44$).

A notable feature of many EBCs (Fig. 5A, left), but not all (Fig. 5A, right), was the structure of head direction tuning between square and circular environments. EBCs would typically have four-pronged directional tuning that aligned with the orientation of the walls in square environments (Fig. 5A, left top). However, as a consequence of consistent egocentric boundary vector tuning in environments of different shapes, EBC tuning yielded directionally uniform tuning in circular environments (Fig. 5A, left bottom).

Figure 5C depicts head direction tuning plots for the full population of RSC neurons recorded in square and circular arenas. When the mean population head direction tuning was examined, distinct peaks fell at the four cardinal directions in square arenas, but no such peaks were observed in their circular counterparts (Fig. 5C, bottom plots). We hypothesized that differences between directional tuning, as a consequence of the presence of EBCs, would allow downstream regions to disambiguate environments of different geometries.

To test this, we trained a linear classifier on a random 80% of the directional tuning curves from both environments and attempted

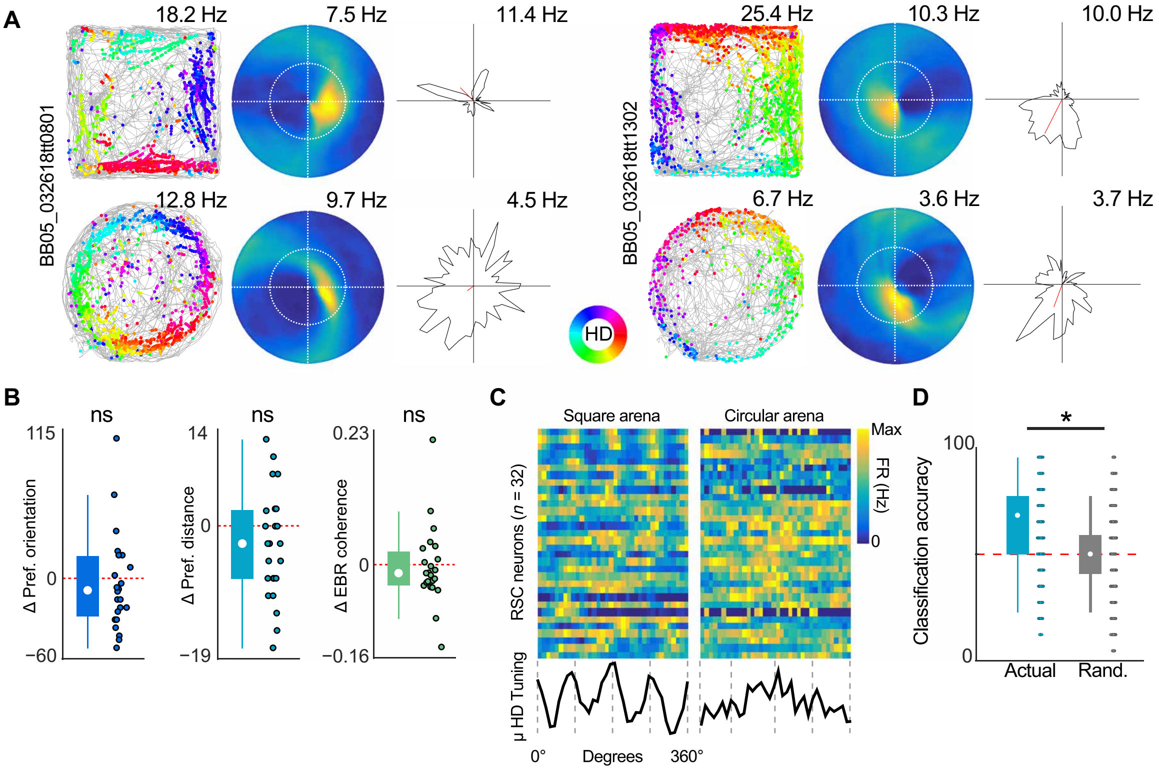

Fig. 5. RSC EBCs are insensitive to environmental geometry, which generates a directional representation of environment shape. (**A**) Trajectory plots, EBRs, and head direction tuning plots for two example RSC EBCs for experimental sessions in a square (top) and circular environment (bottom). (**B**) Preferred orientation, preferred distance, and EBC receptive field coherence from recording sessions in the circular arena subtracted from the corresponding metrics in square arena sessions. (**C**) Head direction tuning plots for all RSC neurons (in the same order) in the square arena (left) and circular arena (right). Color depicts intensity of activation (blue is zero firing rate; yellow is maximum firing rate). Bottom in black: The average head direction tuning across the full population of RSC neurons for the square and circular environments. Gray dashed lines depict 90° axes. (**D**) Arena classification accuracy for linear discriminant analysis on head direction tuning from (C). Teal, actual classification; gray, classification after randomizing arena identity. Red dashed line is statistical chance.

to predict which environment the other 20% of head direction tuning curves were recorded within (Fig. 5D, linear discriminant classifier, $n = 100{,}000$ iterations). Consistent with the hypothesis that geometry could be decoded from a population with EBC tuning, the arena could be identified correctly with 67.7% accuracy (IQR = 50 to 75%), which was statistically significant from both statistical chance (Wilcoxon signed-rank with 50% accuracy median, $z = 218.2$, $P = 0$) and a classifier ran with arena identity randomized (randomized arena identity = 50%; IQR = 41.7 to 58.3%; Wilcoxon rank sum test, $z = 188.4$, $P = 0$). We conclude that regions having egocentric boundary vector tuning may provide punctate directional signals to downstream regions such as the medial entorhinal cortex that can be compared to other directional inputs to inform circuits about environment geometry.

A subpopulation of RSC EBCs are theta-modulated

In building off of geometry detection in RSC EBC ensembles, a natural next question is how might these egocentric positional signals be integrated within the broader spatial circuitry. Previous work has demonstrated that RSC local-field potentials feature a prominent theta oscillation during active movement that is strongly coherent with theta rhythms observed in the dorsal hippocampal formation (*34*, *35*). Spatial representations in regions with strong theta rhythmicity, such as medial entorhinal cortex or hippocampus, are strongly influenced by boundaries and environmental geometry (*36*–*41*). We next questioned whether RSC neurons exhibiting egocentric boundary vector sensitivity were potentially synchronized with these areas via theta oscillations.

Consistent with previous work, we observed a strong RSC theta oscillation and that individual RSC neurons engaged with the theta oscillation (Fig. 6, A and B). A small subpopulation of RSC neurons exhibited theta rhythmic spiking (as revealed by autocorrelations of their spike trains) and were phase-locked to the locally recorded theta oscillation (Fig. 6B; 4%, $n = 22/555$). A larger subset of RSC neurons did not have detectable theta rhythmic spiking but were significantly phase-locked to the theta oscillation (Fig. 6C; 27.6%, $n = 153/555$, see Materials and Methods).

Virtually no EBCs exhibited intrinsically theta rhythmic spiking (0.08%, $n = 1/134$), but 25.4% of EBCs ($n = 34/134$) were phase-locked to RSC theta oscillations (Fig. 6D). The strength of theta modulation (MRL) was similar for theta-modulated non-EBCs and EBCs (Fig. 6E, non-EBC MRL = 0.13, IQR 0.10 to 0.18; EBC MRL = 0.11, IQR = 0.09 to 0.14, Wilcoxon rank sum test, $z = 1.59$, $P = 0.11$). Non-EBC theta-locked RSC neurons were biased to firing during the rising phase of the theta rhythm, whereas theta-locked EBCs preferred the falling phase (Fig. 6F, non-EBCs phase = 3.55 rad, IQR = 1.94 to 4.87 rad; EBCs phase = 2.31 rad, IQR = 1.64 to 5.07 rad; Watson-Williams test, $F = 45.4$, $P = 3.14 \times 10^{-10}$). These results confirm that a subpopulation of RSC EBCs are phase-locked to theta oscillations present in RSC, consistent with recent modeling work

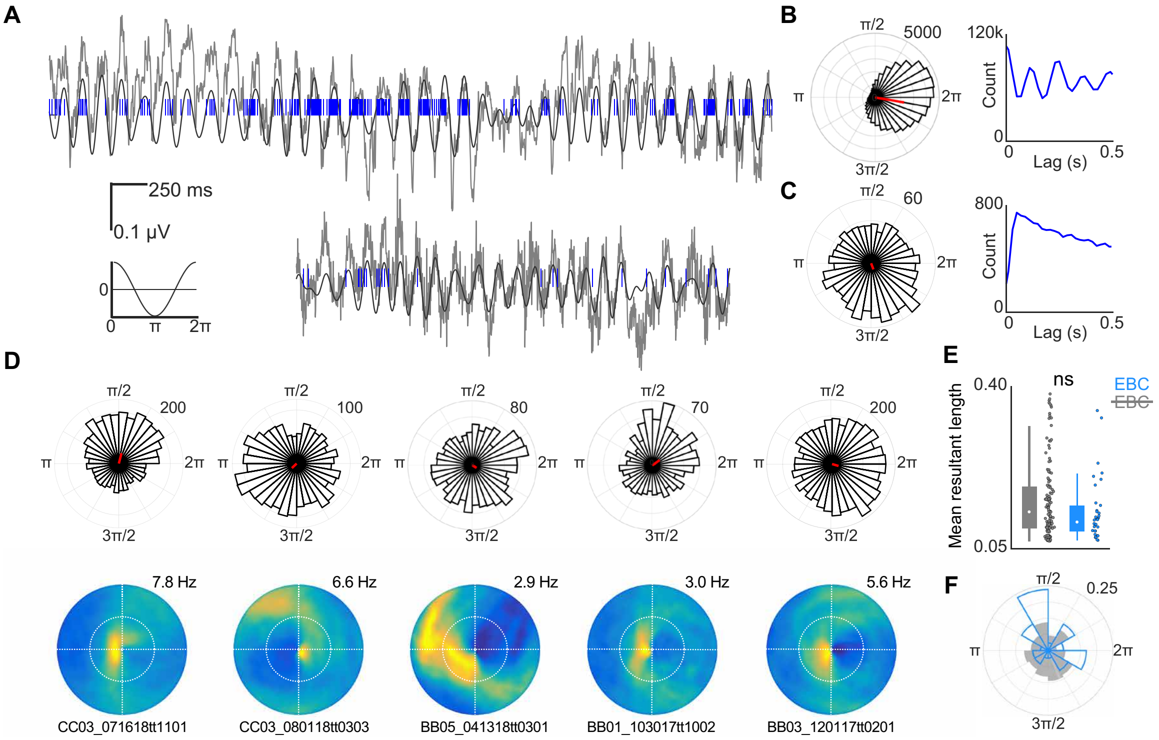

Fig. 6. A subset of RSC EBCs is theta-modulated. (**A**) Two examples of RSC theta oscillation (gray) and spike train of simultaneously recorded neurons (blue). Bottom left: Scale bar and schematic depicting correspondence between oscillation and theta phase. (**B**) Left: Circular histogram depicting spike counts as a function of theta phase for the neuron in the top row of (A). Density of spikes near 2π indicates that the neuron is locked to the peak of the theta phase. Right: Spike train autocorrelogram for the same neuron shows theta rhythmic spiking. (**C**) Same as in (B) but for the neuron depicted in the bottom row of (A). This neuron is significantly theta phase-modulated but does not exhibit theta rhythmic spiking. (**D**) Example theta phase-modulated EBCs. Top row: Circular histogram of spike counts versus theta phase. Bottom row: Corresponding EBRs. (**E**) Strength of theta phase modulation as measured by the MRL for non-EBCs (gray) and EBCs (blue). EBCs have theta modulation significantly similar to non-EBCs with significant phase relationships. (**F**) Preferred theta phase for all EBCs (blue) and non-EBCs (gray). EBCs tended to prefer the falling phase of the theta oscillation, while non-EBCs preferred the rising phase.

suggesting periodic modulation as a mechanism for comparing current sensory input about the environment against stored spatial representations (*7*).

DISCUSSION

RSC spatial representations facilitate reference frame transformations

The current data support and extend the functional role of RSC in reference frame transformations. Specifically, the RSC population exhibits sensitivity to multiple spatial coordinate systems, an essential characteristic of circuitry capable of generating such translations. In the current work, we report a large subset of spatially reliable neurons that encode the position of boundaries in egocentric coordinates. Referred to as EBCs, these neurons robustly encoded a vectorial representation of the distance and orientation of any boundary relative to the animal itself (i.e., in an egocentric reference frame) (*15*, *16*, *17*, *19*). Egocentric boundary representations are predicted to form a critical component of the coordinate transformation circuit, as the response property could function to inform the broader spatial circuitry about the position of external landmarks in a viewpoint-dependent manner (*7*, *8*).

RSC neurons also exhibited multiple forms of allocentric modulation. Nearly half of RSC neurons exhibited reliable and spatially anchored responses during free foraging behavior. Spatially stable cells had complex 2D spatial representations that, in some cases, were reminiscent or possibly descended from spatial non-grid cells observed in medial entorhinal cortex (*42*), allocentric boundary vector cells and axis-tuned neurons of dorsal subiculum (*43*–*45*), and/or location-modulated head direction cells of post-subiculum (*18*). A second form of allocentric response was observed in a subset of RSC neurons that exhibit allocentric head direction sensitivity. These forms of allocentric spatial information may be processed or compared with egocentric boundary vector information within theta time scales. Both subsets of neurons exhibited theta phase modulation, which is well known to synchronize information processing throughout the broader allocentric spatial circuit.

When paired with the unique anatomical connectivity of RSC with both egocentric and allocentric processing regions, the presence of neurons, such as EBCs, that are sensitive to one or more spatial coordinate systems signifies that the region is capable of interrelating external and internal spatial information for the initial construction and use of stored spatial representations. This fact may explain the diversity of impairments observed in spatial navigation, learning, and memory that occur following damage, lesion, or inactivation of the area (*46*).

The RSC egocentric boundary vector code is context independent, which generates a directional code that reflects environment geometry

EBC spatial receptive fields were activated when the animal was positioned with both a specific orientation and distance from an environmental boundary. EBCs maintained their preferred vector tuning preference in rotated, expanded, and novel arenas (Fig. 4). Accordingly, the EBC signal does not remap across environments, thus providing a stable, context invariant, positional metric.

This stability can be contrasted to the vast majority of allocentric representations, such as place cells, grid cells, or head direction cells, that are known to either show global or rate remapping, translations, or rotations between environments (*36*, *47*, *48*). In contrast, border cells of medial entorhinal cortex and boundary vector cells of dorsal subiculum maintain similar tuning preferences in a context invariant manner analogous to that observed in the EBCs shown here (*41*, *44*). It remains to be seen what interactions exist between cells having these different types of boundary-anchored receptive fields; however, the current data suggest that boundary-sensitive neurons may provide a foundational map upon which other spatial representations can be situated.

Like border and boundary vector cells, RSC EBC vector representations did not remap in environments of different geometries (*41*, *44*). However, because EBCs respond in a directionally dependent manner along every environmental border, the mean directional tuning of the RSC population reflected the shape of the environment (Fig. 5). Here, we demonstrated that this directional signal could be used to distinguish arena shape. Relative positions of boundaries have repeatedly been shown to alter or anchor allocentric spatial representations, especially in medial entorhinal grid and hippocampal place cells (*36*–*40*, *49*). Medial entorhinal cortex receives excitatory projections, both directly and indirectly, from RSC and projects into hippocampus. We hypothesize that the RSC arena geometry–related directional signal may serve to provide excitatory drive at specific allocentric head directions to inform the circuit about the relative angles among borders.

The invariance of EBC response fields and their relationship to environmental geometry may also support or drive route-referenced spatial representations observed in RSC and parietal cortex, which are anchored to space as defined by the route itself (*27*, *29*, *50*). These route-centric activity patterns are often modulated by the geometric shape of the trajectory, which could be partially explained by EBCs responding to specific environmental features such as corners, repeating egocentric views, or some conjunction of EBC responsivity and other spatial covariates (*9*, *26*, *51*). Accordingly, future work is needed to assess the relationship between EBC sensitivity in the open field and responses of RSC and parietal cortex in linearized environments.

EBCs are primarily restricted to the dysgranular RSC

A notable anatomical feature of the EBC population was that it was primarily localized to the dysgranular subregion of RSC. Dysgranular RSC has connectivity weighted toward egocentric coordinate systems, as it is reciprocally innervated by cortical regions important for processing sensory and motor information as well as association areas such as parietal cortex wherein egocentrically referenced spatial responses have been observed (*9*, *13*, *14*, *20*). Further, the concentration of EBCs in dysgranular RSC is consistent with theoretical work proposing a circuit for translating between egocentric and allocentric coordinate systems that includes parietal cortex, RSC, and the extended hippocampal formation as primary hubs (*7*, *8*, *21*, *22*).

Of note, dysgranular RSC was shown by Jacob *et al.* to have bidirectional head direction cells that respond to local reference frames in multicompartment environments with distinct contextual cues (*33*). This sensitivity ultimately yields allocentric directional tuning plots that are bimodal. In the current work, strongly tuned EBCs commonly exhibited quad-modal allocentric directional tuning that was aligned with the four walls of square environments. This similarity in directional tuning response of EBCs and bidirectional head direction cells and their colocalization in dysgranular RSC raises questions as to the nature of the relationship or interactions between these functional subpopulations.

One possibility is that neurons in dysgranular RSC are prone to represent the locations of spatial landmarks using egocentric vectors and that EBCs and bidirectional head direction cells are both special cases constrained by their respective experimental setups. In the case of EBCs reported here, the vector may anchor to boundaries because borders are the only landmarks present in the open field that can cause activation of the receptive field. In the work of Jacob *et al.*, the egocentric vector may respond to borders as well as local visual landmarks or doorways between two compartments. The bimodal directional tuning in the latter experiment may arise from constrained egocentric sampling along two axes as a consequence of the multicompartment environment segmenting two opposing walls. This proposed egocentric vector encoding of environment features in RSC may underlie functional correlates of local heading orientation, scene processing, or goal location in RSC in humans (*52*–*55*).

A network of vector-based egocentric spatial representation

In addition to RSC, EBCs were also observed in both parietal and secondary motor cortices (M2) but not medial entorhinal cortex, which is commonly thought to represent space in allocentric coordinates. The presence of EBCs in parietal cortex converges nicely with previous work, demonstrating egocentric bearing sensitivity of neurons within the region to visual cues positioned along boundaries (*20*). Computational models exploring circuitry for reference frame transformations and spatial imagery initially predicted EBCs to exist in parietal cortex (*8*). However, egocentric responses were initially reported in lateral entorhinal cortex, dorsal striatum, and postrhinal cortex (*15*–*17*, *19*) and now, here in RSC, parietal cortex and M2. Accordingly, a picture of a distributed network of interconnected regions with egocentric vector representations is beginning to emerge. Given the presence of EBCs in several midline structures, it is possible that EBCs are also present in the anterior cingulate cortex as well as thalamic structures that innervate midline associative cortex. In the current report, we observe lateralization of the preferred orientation of EBC receptive fields that is contralateral with the hemisphere that the neuron is within. This may offer clues as to the origin of the egocentric signal. Specifically, it suggests that EBCs are likely to be driven directly by contralaterally projecting thalamic afferents or early cortical processing regions, which also have this form of lateralization. Regardless, future investigations should focus on dependencies among the regions currently implicated, as the EBC network may have functional and anatomical connectivity resembling the well-characterized extended head direction cell network.

MATERIALS AND METHODS

Subjects

Male Long-Evans rats ($n = 7$; Charles River Laboratories, Wilmington, MA) were housed individually in plexiglass cages and kept on a 12-hour light/dark cycle. Rats had continuous access to food during a habituation period lasting approximately 1 week. After this period, animals were food-restricted until they reached 85 to 95% of their weight during free feeding. Water was available continuously. All procedures were approved by the Institutional Animal Care and Use Committee at Boston University.

Shaping/behavior

Animals were acclimated to the primary testing room for approximately 1 week. During acclimation, rats were handled by multiple researchers and trained to consume both Froot Loops (General Mills, Battle Creek, MI) and 45 mg of chocolate pellets (Bio-Serv, Flemington, NJ). After animals readily ate both food items, they were exposed to one of two familiar open fields used for baseline sessions. The first open field was 1.25 m^2 with four black walls 30 cm in height. The second arena was 1.25 m^2 with three black walls and one white wall 30 cm in height. Both arenas were placed on a dark gray textured rubber floor that was cleaned between sessions. Two animals performed a goal-directed navigation task in a different arena and testing room before being used for the current study.

Surgical procedures

Rats were surgically implanted with custom-fabricated hyperdrives in aseptic conditions. Each hyperdrive was composed of 12 to 16 nickel chromium tetrodes (12 μm, Kanthal-Sandvik, Hallstahammar, Sweden) that could be independently moved in as small as 35-μm increments. Guide cannulae for each tetrode were collectively configured in one of three arrays: (i) filling a single hypodermic tube approximately 2 mm^2 in diameter, (ii) across two conjoined hypodermic tubes that were ~1.5 mm^2 in diameter spanning a total of ~3 mm or, (iii) across four conjoined hypodermic tubes that were ~1.25 mm^2 in diameter and spanned a total of ~5 mm. For the second and third configurations, the long axis of the electrode array was positioned to target an extended region of the anterior-posterior axis of RSC.

Animals were anesthetized using a combination of inhaled isoflurane (0.5% initial concentration) and ketamine/xylazine administered via intraperitoneal injection (ketamine: 12.92 mg/kg, acepromazine: 0.1 mg/kg, xylazine: 1.31 mg/kg). After the animal was determined to be under anesthesia (as assessed via loss of the toe-pinch reflex), the animal was positioned in a stereotaxic apparatus, a dose (0.1 mg/kg) of atropine was administered subcutaneously, and the head was shaved. Excess hair was removed via application of Nair (Church & Dwight Co., Ewing, NJ), and the scalp was cleaned with 70% ethanol and Betadine (Avrio Health L.P., Stamford, CT). Sodium chloride (0.9%) was administered subcutaneously hourly throughout the surgical procedure.

Following a midline incision and subsequent clearing of connective tissue, a ground screw was positioned above the cerebellum, and five to eight anchor screws were affixed in an array around the perimeter of the exposed skull. A large craniotomy was centered above RSC (relative to bregma: A/P: −2 mm to −7 mm; M/L: ±0 to 1.75 mm). The exact size and position of the craniotomy was dependent on the aforementioned configuration of the hyperdrive array. Next, dura was resected and the hyperdrive was positioned such that guide cannula rested gently against the dorsal surface of the brain. Excess exposed tissue within the craniotomy was protected with Kwik-Sil (World Precision Instruments, Sarasota, FL), and the implant was secured to anchor screws with dental cement. Tissue around the implant was cleaned with saline, 70% ethanol, and hydrogen peroxide. Antibiotic ointment was applied into the wound and sutured if necessary, and Neosporin was applied around the site. Before removal from anesthesia, tetrodes were lowered approximately 0.25 mm dorsal/ventral. Animals received post-operative antibiotics (Baytril: 10 mg/kg) and analgesics (Ketofen: 5.0 mg/kg) for 5 days after surgery and were freely fed. One week after operation, animals were handled and reacclimated to the testing room and free foraging environments before the initiation of experiments.

Electrophysiological recordings

Neural signals were amplified at two headstages attached to a 64-channel electrical interface board and acquired by a 64-channel Digital Lynx acquisition system (Neuralynx, Bozeman, MT). Signals were digitized, filtered (0.3 to 6.0 kHz), and amplified (5000 to 20,000×). Timestamps of individual action potentials were detected online when the signal crossed an acquisition threshold on any individual electrode composing a tetrode. At the conclusion of each experiment, spikes were manually sorted to individual single units using Offline Sorter (Plexon Inc., Dallas, TX) and the following features: peak-valley, peak, and principal components 1 to 3. Two diodes attached to the electrode implant delineated the location of the animal, which was tracked at 30 Hz via a camera positioned above the recording arena.

An experimental session began with an initial 15- to 30-min recording, while the animal free explored and consumed either Froot Loops scattered by an experimenter, chocolate pellets released at random intervals from a dispenser positioned above the arena, or both (Open Ephys Pellet Dispenser designed by Maurer Lab, https://github.com/jackpkenn/PelletDispenser). After adequate spatial coverage was achieved, the animal was removed from the arena and placed back in its home cage for a period of 1 hour minimally. During this period, the experimenter completed clustering of action potentials into single neurons and examined 2D spatial ratemaps (described below) to assess whether any of the cells from the baseline session exhibited egocentric boundary vector sensitivity. If no EBCs were present, tetrodes were typically lowered between 35 and 70 μm. If EBCs were present, a second experimental session was conducted in which the animal explored an open field in one or more of the following configurations:

1) Open-field session: The same arena from the baseline session to assess the stability of EBCs in familiar environments.

2) Open-field rotation: The same arena from the baseline session rotated 45° relative to the testing room and all visible distal cues present therein.

3) Circular open field: A familiar circular arena of 1.2-m diameter.

4) Open-field expansion or contraction: If an expansion experiment was planned, the initial baseline session was conducted in a familiar 1.25-m^2 arena that enabled reconfiguration of walls. Following the baseline session, walls were uniformly moved outward relative to the center point of the baseline configuration to a size of 1.5 m^2 or larger. In a small number of recordings, walls were either moved nonuniformly to increase the length of the arena along a single axis of the environment or contracted to decrease the size of the environment. Across all possible wall movements, the arena was altered in size by approximately 20% along each dimension.

5) No wall open field: If a no wall arena experiment was planned, the initial baseline session was conducted in a familiar 1.25-m^2 environment that was placed approximately 20 cm above the floor. Following this session, the walls were removed from this arena, creating a platform with no walls that the rat explored for a second time. In a small number of sessions, the animal explored the familiar 1.25-m^2 environment that was situated on the testing room floor and then, in a second session, explored a different familiar arena lacking walls placed approximately 20 cm above the floor.

All arenas were positioned such that the animal could easily see the broader recording room and an array of stable distal cues. In some cases, the manipulation session was followed by a return session to the familiar baseline arena.

Histology

Animals were anesthetized with 0.5% isoflurane, and small electrical lesions were made at the end of tetrodes that had preliminarily been identified as having EBCs. After 1 week, animals were deeply anesthetized with isoflurane, injected with sodium pentobarbital, and transcardially perfused with 0.9% saline followed by 10% formalin. The brain was extracted from the skull and post-fixed overnight with 10% formalin and then stored in 0.1 M phosphate buffer until 2 days before slicing when it was transferred to a 0.1 M phosphate buffer/30% sucrose solution. The brain was snap-frozen using 2-methylbutane and sliced into 40- to 50-μm coronal sections using a cryostat (Leica CM3050S, Leica Biosystems, Buffalo Grove, IL). Slices were mounted on gelatin-covered microscope slides and allowed to dry and then photographed (Nikon DXM1200 camera mounted on Olympus BX51 light microscope). Tetrode lesions and tracts were clearly visible in all animals. Coordinates of tetrode locations and final tetrode depths were registered with respect to pre-implant photographs of guide cannulae array configurations and tetrode turning logs, respectively. Medial entorhinal cortex recordings and tetrode verifications were previously verified and reported (*56*).

Data analysis

2D spatial ratemaps and spatial stability

Animal positional occupancy within an open field was discretized into 3 cm × 3 cm spatial bins. For each neuron, the raw firing rate for each spatial bin was calculated by dividing the number of spikes that occurred in a given bin by the amount of time the animal occupied that bin. Raw firing ratemaps were smoothed with a 2D Gaussian kernel spanning 3 cm to generate final ratemaps for visualization. Individual raw firing ratemaps were also computed after dividing the session into halves. To assess spatial stability of an individual RSC neuron, the similarity of the two raw firing ratemaps from nonoverlapping halves of the recording session was calculated using the nonparametric Spearman's rank correlation coefficient. To determine whether a given spatial stability value was greater than expected by chance, we next conducted randomization tests wherein the spike train for each RSC neuron was circularly shifted relative to spatial position 100 times, and individual firing ratemaps were constructed for nonoverlapping halves that were then correlated. The spatial stability correlation values following randomizations were collapsed into a single distribution for all neurons and randomizations, and the 99th percentile of all values was calculated. RSC neurons with real spatial stability correlations greater than this threshold were determined to have robust 2D spatial stability.

Construction of EBRs

EBRs were computed in a similar manner as 2D spatial ratemaps but referenced relative to the animal rather than the spatial environment. The position of the boundaries relative to the animal was calculated for each position sample (i.e., frame). For each frame, we found the distance, in 2.5-cm bins, between arena boundaries and angles radiating from 0° to 360° in 3° bins relative to the rat's position. Critically, angular bins were referenced to the head direction or movement direction of the animal such that 0°/360° was always directly in front of the animal, 90° to its left, 180° directly behind it, and 270° to its right. Intersections between each angle and environmental boundaries were only considered if the distance to intersection was less than or equal to one-half the length of the most distant possible boundary (in most cases, this threshold was set at 62.5 cm or half the width of the arena). In any frame, the animal occupied a specific distance and angle relative to multiple locations along the arena boundaries, and accordingly, for each frame, the presence of multiple boundary locations was added to multiple 3° × 2.5 cm bins in the egocentric boundary occupancy map. The same process was completed with the locations of individual spikes from each neuron, and an EBR was constructed by dividing the number of spikes in each 3° × 2.5 cm bin by the amount of time that bin was occupied in seconds. Smoothed EBRs were calculated by convolving each raw EBR with a 2D Gaussian kernel (5 bin width, 5 bin SD).

For EBR construction and other analyses in the current work, head direction was the instantaneous angle calculated from the location of two position tracking diodes, and movement direction was defined as the instantaneous derivative of the position signal. Head direction was used as the primary directional variable in EBR construction, but a comparison to movement direction determined the latter to be a less robust signal for egocentric boundary vector tuning. However, some neurons showed significant egocentric boundary tuning in relationship to movement direction rather than head direction.

Head direction cell identification

For each neuron, the MRL of the firing rate as a function of head direction was calculated as

$$R_{\mathrm{m}} = \frac{\cos(\overline{\theta})\sum_{i=1}^{n} F_i \cos(\theta_i) + \sin(\overline{\theta})\sum_{i=1}^{n} F_i \sin(\theta_i)}{\sum_{i=1}^{n} F_i}$$

where $\overline{\theta}$ was the head direction of firing and F_i and θ_i were the firing rate and head direction for bin *i*. Head direction cells were identified as those cells with R_{m} greater than 0.20. Head direction cells ($n = 27/555$; 4.9% of all RSC neurons) were removed from the possible pool of RSC EBCs.

Identification of neurons with egocentric boundary vector tuning

To identify neurons with significant egocentric boundary vector sensitivity, we began by calculating the mean resultant (MR) of the cell's egocentric boundary directional firing collapsed across distance to the boundary. The mean resultant was calculated as

$$\mathrm{MR} = \left(\sum_{\theta=1}^{n}\sum_{D=1}^{m} F_{\theta,D} * e^{i*\theta}\right) / (n*m)$$

where θ is the orientation relative to the rat, *D* is the distance from the rat, $F_{\theta,D}$ is the firing rate in a given orientation-by-distance bin, *n* is the number of orientation bins, *m* is the number of distance bins, *e* is the Euler constant, and *i* is the imaginary constant. The MRL is defined as the absolute value of the mean resultant and characterized the strength of egocentric bearing tuning to environment boundaries. We next computed the preferred orientation of the EBR as the mean resultant angle (MRA)

$$\mathrm{MRA} = \arctan2\left(\frac{\mathrm{imag(MR)}}{\mathrm{real(MR)}}\right)$$

We estimated the preferred distance by fitting a Weibull distribution to the firing rate vector corresponding to the MRA and finding the distance bin with the maximum firing rate. The MRL, MRA, and preferred distance were calculated for each neuron for the two halves of the experimental session independently. Next, the MRL was computed for each neuron following 100 random, unrestricted, circular shifts of the spike train relative to position. The 99th percentile of the MRL distribution across all neurons was determined.

A neuron was characterized as having egocentric boundary vector tuning (i.e., an EBC) if it reached the following criteria: (i) the MRL from the baseline session was greater than the 99th percentile of the randomized distribution, (ii) the absolute circular distance in preferred angle between the first and second halves of the baseline session was less than 45°, and (iii) the change in preferred distance for both the first and second halves relative to the full session was less than 50%.

To refine our estimate of the preferred orientation and preferred distance of each neuron, we calculated the center of mass of the receptive field defined after thresholding the entire EBR at 75% of the peak firing and finding the largest continuous contour ("contour" in MATLAB). We repeated the same process for the inverse EBR for all cells to identify both an excitatory and inhibitory receptive field and corresponding preferred orientation and distance for each neuron.

Ratemap coherence, dispersion, and receptive field size

For either EBRs or 2D spatial ratemaps, coherence was defined as the Spearman's correlation between each spatial bin and the mean firing rate of all adjacent bins. Dispersion was calculated as the mean within ratemap distance of the top 10% of firing rate bins. Receptive field size was only calculated for EBRs (described below) and was defined by the area (percentage of all EBR degree × cm bins) of the largest single contour detected after selecting for bins with firing rates greater than 75% of the maximum firing rate.

Self-motion ratemaps and assessment of self-motion sensitivity

Angular displacement (θ) was calculated by determining the circular difference in movement direction between two position samples (frames) separated by a 100-ms temporal window. The total distance (*d*) traveled between these two frames was also calculated. The process was repeated for the full recording by sliding a 100-ms temporal window across all position frames and calculating these values. Angular displacement and distance traveled were converted to Cartesian coordinates to generate *x*- and *y*-displacement values in centimeters, which corresponded to lateral and longitudinal displacements for each frame across the full recording.

2D displacements were binned (1 cm) and convolved with a 2D Gaussian spanning 3 cm. For each neuron, the same process was repeated for displacement values that co-occurred with spike times to generate a spike occupancy map as a function of displacement. Self-motion ratemaps were constructed by dividing the spike occupancy map for each neuron by the total time in each displacement bin. Bins occupied for less than 267 ms were removed from analyses, as they typically were observed at extreme displacement values. Self-motion ratemaps for each neuron were additionally constructed independently from interleaved, nonoverlapping, 1-s periods throughout the entire session to assess stability of self-motion tuning. For quantification of self-motion tuning relative to a randomized distribution, all aforementioned ratemaps were generated for each neuron 100 times after randomly shifting the spike train relative to position.

Self-motion ratemaps were quantified for their stability, left- versus right-turning preference (LvR), and "speed" modulation. First, stability of self-motion tuning was quantified by correlating self-motion ratemaps generated from nonoverlapping periods for each neuron (Fig. 2B). Next, turning biases for clockwise versus counterclockwise movements (LvR FR ratio, Fig. 2C) were quantified by computing the ratio of summated firing for all similarly occupied displacement bins on the right and left sides of the zero vertical line, respectively. Last, speed modulation was approximated by finding the mean firing rate as a function of longitudinal displacement (i.e., averaging over columns of self-motion ratemaps) and correlating with the *y*-displacement value (Fig. 2D). All self-motion ratemap quantification was repeated for all randomized self-motion ratemaps as mentioned above. Stability and turn-bias quantification were computed from displacement bins that were occupied in both self-motion ratemaps or both halves of an individual self-motion ratemap. All quantification was completed on nonsmoothed self-motion ratemaps.

Generalized linear models

To more directly test to what degree neurons represented egocentric compared to allocentric variables, we adopted a GLM framework. The probability of spiking in a given behavioral frame (33 Hz) is described by an inhomogeneous Poisson process, where the probability of spiking in a given frame is described by the time varying variable λ

$$P(\text{Spike} \mid t) = e^{-\lambda(t)}$$

$$\lambda(t) = \lambda_{\text{FR}} * \lambda(t)_{\text{SelfMovement}} * \lambda(t)_{\text{Egocentric}}$$

where

$$\lambda_{\text{FR}} = \beta_0$$

$$\lambda_{\text{SelfMovement}}(t) = v_1 S + v_2 A$$

$$\lambda_{\text{Allocentric}}(t) = \rho_1 x + \rho_2 y + \rho_3 x^2 + \rho_4 y^2 + \rho_3 xy + \rho_6 \cos(\varphi) + \rho_7 \sin(\varphi)$$

$$\lambda_{\text{Egocentric}}(t) = \varepsilon_1 d + \varepsilon_2 d^2 + \varepsilon_3 \sin(\theta) + \varepsilon_4 \cos(\theta) + \varepsilon_5 \mathrm{d} * \sin(\theta) + \varepsilon_6 \mathrm{d} * \cos(\theta)$$

where β_0 defines the baseline firing rate of the neuron. All subscripted variables are fit coefficients weighting the other (time-varying) variables. S is the running speed of the animal, and A is the angular displacement of the animal, as described above. x and y are measurements of the animal's position in the environment in pixels, and φ is the head direction. Last, d is the animal's distance from the center of the environment, and θ is the egocentric angle to the center of the environment.

Coefficients were determined by fitting to maximize log-likelihood (MATLAB function "glmfit") of the experimental spike train given the behavioral variables. For statistical tests, some numbers of the coefficients were set to zero, giving a log-likelihood for the reduced model. The difference in likelihood for the full versus reduced model was compared to a chi-square distribution (degrees of freedom equal to the number of coefficients set to zero) to generate an analytic *P* value. While theoretically the change in log-likelihood should follow a chi-square distribution, this is only the case when the spike train has been fit very well (e.g., including all neuron-neuron coupling terms). In line with previous approaches, we therefore also compared the change in log-likelihood in two additional manners. First, we compared the change in log-likelihood to that from 1000 randomly shuffled spike train, giving an empirical null distribution. Second, when comparing the relative effects of two variables (that is, comparing two reduced models to each other), we can derive the dAIC for each of the reduced models and compare their magnitudes. Representative spike trains for each model were generated by evaluating lambda for each behavioral time point ("glmeval" in MATLAB) and using this as the input to a random Poisson generator ("poissrnd" in MATLAB).

Classification of arena shape condition from directional tuning

Head direction tuning curves were calculated for each neuron ($n = 32$) by normalizing the number of spikes occurring in a given 10° directional bin by the amount of time that bin was occupied. Head direction tuning curves were independently calculated for sessions in square and circular environments and normalized by peak firing rate. Directional tuning curves were labeled with the arena condition in which they were sampled and classified. Tuning curves were down-sampled to include alternating directional bins (every 20°, to ensure the covariance matrix would be positive definite) and then classified using linear discriminant analysis 100,000 times for arena condition with cross-validation (80% train, 20% test; "classify" in MATLAB) and uniform priors. Classification accuracy was assessed by finding the percentage of correct labels on the test dataset. A randomized distribution of classification accuracy was calculated in parallel by randomizing the true arena condition label of the training set.

Assessment of theta phase modulation

For each experimental session, an local field potential (LFP) channel was identified that was qualitatively noise free. The LFP signal was filtered in the theta frequency range (6 to 10 Hz), and the phase for each spike from each neuron was estimated as the instantaneous phase angle of the corresponding Hilbert transform ("hilbert" in MATLAB). For each neuron, the MRL and MRA were calculated on the full spike phase distribution using the circular statistics toolbox (Berens *et al.*, 2009; MRL, "circ_r"; MRA, "circ_mean"). We next randomly shifted the spike train relative to theta phase 100 times for each neuron to generate a null distribution of MRL values. RSC neurons with MRLs greater than the 95th percentile of the full distribution of randomized MRL values were determined to be theta phase–locked.

Assessment of theta rhythmic spiking

Spike train autocorrelograms were estimated by generating a histogram of temporal lags between spikes in a 400-ms temporal window discretized into 20-ms bins. For each neuron, the power spectrum of the autocorrelogram was computed using the Fourier transform ("fft" in MATLAB), and the peak in the theta frequency range was identified (if it existed). If the mean power within 1 Hz of this theta peak was 50% greater than the mean power for the full power spectrum, the neuron was determined to exhibit intrinsic theta spiking.

Von Mises mixture models

Distribution of preferred orientation estimates was modeled as mixtures of Von Mises distributions using orders from 1 to 5 ("fitmvmdist" found at https://github.com/chrschy/mvmdist). Optimal models were identified as the model increasing model fit over the one-component model with the next complex model yielding less improvement. Models were cross-validated using randomly selected halves of the preferred orientation distribution. Theta of each Von Mises component is reported, and a distribution function of the optimal model was generated to visualize mixture model fit.

Statistics

Unless otherwise stated, nonparametric tests with a *P* value threshold at 0.05 were used for all statistical comparisons. Median and IQR are provided for all distributions in which comparisons were made.

Data and code availability

The toolbox used for alignment of behavioral and spike data, along with basic analysis, is available at https://github.com/hasselmonians/CMBHOME. The toolbox used for EBR generation and related analyses is available at https://github.com/hasselmonians/EgocentricBoundaryCells. The toolbox used for GLM fits, evaluation, and spike-train generation is available at https://github.com/wchapman/pippin. All other analysis code will be made available upon request from the corresponding author.

SUPPLEMENTARY MATERIALS

Supplementary material for this article is available at http://advances.sciencemag.org/cgi/content/full/6/8/eaaz2322/DC1

Fig. S1. Locations of RSC EBCs and identification as putative principal cells.

Fig. S2. RSC spatial stability during free foraging.

Fig. S3. Comparison of EBCs detected using head direction versus movement direction.

Fig. S4. VMM fits to distribution of preferred orientation.

Fig. S5. Simultaneously recorded EBCs.

Fig. S6. EBCs in M2 cortex and posterior parietal cortex but not medial entorhinal cortex.

Fig. S7. Egocentric vector tuning to center of arena for GLMs.

Fig. S8. EBC detection decreases as threshold for allowed variability in preferred distance becomes more conservative.

REFERENCES AND NOTES

1. T. Hafting, M. Fyhn, S. Molden, M.-B. Moser, E. I. Moser, Microstructure of a spatial map in the entorhinal cortex. *Nature* **436**, 801–806 (2005).
2. J. O'Keefe, J. Dostrovsky, The hippocampus as a spatial map. Preliminary evidence from unit activity in the freely-moving rat. *Brain Res.* **34**, 171–175 (1971).
3. J. S. Taube, R. U. Muller, J. B. Ranck Jr., Head-direction cells recorded from the postsubiculum in freely moving rats. I. Description and quantitative analysis. *J. Neurosci.* **10**, 420–435 (1990).
4. R. G. M. Morris, P. Garrud, J. N. P. Rawlins, J. O'Keefe, Place navigation impaired in rats with hippocampal lesions. *Nature* **297**, 681–683 (1982).
5. H.-A. Steffenach, M. Witter, M.-B. Moser, E. I. Moser, Spatial memory in the rat requires the dorsolateral band of the entorhinal cortex. *Neuron* **45**, 301–313 (2005).
6. R. A. Andersen, G. K. Essick, R. M. Siegel, Encoding of spatial location by posterior parietal neurons. *Science* **230**, 456–458 (1985).
7. A. Bicanski, N. Burgess, A neural-level model of spatial memory and imagery. *eLife* **7**, e33752 (2018).
8. P. Byrne, S. Becker, N. Burgess, Remembering the past and imagining the future. *Psychol. Rev.* **114**, 340–375 (2007).
9. J. R. Whitlock, G. Pfuhl, N. Dagslott, M.-B. Moser, E. I. Moser, Functional split between parietal and entorhinal cortices in the rat. *Neuron* **73**, 789–802 (2012).
10. M.-L. Mittelstaedt, H. Mittelstaedt, Homing by path integration in a mammal. *Naturwissenschaften* **67**, 566–567 (1980).
11. J. Cho, P. E. Sharp, Head direction, place, and movement correlates for cells in the rat retrosplenial cortex. *Behav. Neurosci.* **115**, 3–25 (2001).
12. J. R. Hinman, M. P. Brandon, J. R. Climer, G. W. Chapman, M. E. Hasselmo, Multiple running speed signals in medial entorhinal cortex. *Neuron* **91**, 666–679 (2016).
13. B. L. McNaughton, S. J. Mizumori, C. A. Barnes, B. J. Leonard, M. Marquis, E. J. Green, Cortical representation of motion during unrestrained spatial navigation in the rat. *Cereb. Cortex* **4**, 27–39 (1994).
14. A. A. Wilber, I. Skelin, W. Wu, B. L. McNaughton, Laminar Organization of Encoding and Memory Reactivation in the Parietal Cortex. *Neuron* **95**, 1406–1419 (2017).
15. X. Gofman, G. Tocker, S. Weiss, C. N. Boccara, L. Lu, M.-B. Moser, D. Derdikman, Dissociation between postrhinal cortex and downstream parahippocampal regions in the representation of egocentric boundaries. *Curr. Biol.* **29**, 2751–2757.e4 (2019).
16. J. R. Hinman, G. W. Chapman, M. E. Hasselmo, Neuronal representation of environmental boundaries in egocentric coordinates. *Nat. Commun.* **10**, 2772 (2019).
17. P. A. LaChance, T. P. Todd, J. S. Taube, A sense of space in postrhinal cortex. *Science* **365**, eaax4192 (2019).
18. A. Peyrache, N. Schieferstein, G. Buzsáki, Transformation of the head-direction signal into a spatial code. *Nat. Commun.* **8**, 1752 (2017).
19. C. Wang, X. Chen, H. Lee, S. S. Deshmukh, D. Yoganarasimha, F. Savelli, J. J. Knierim, Egocentric coding of external items in the lateral entorhinal cortex. *Science* **362**, 945–949 (2018).
20. A. A. Wilber, B. J. Clark, T. C. Forster, M. Tatsuno, B. L. McNaughton, Interaction of egocentric and world-centered reference frames in the rat posterior parietal cortex. *J. Neurosci.* **34**, 5431–5446 (2014).
21. B. J. Clark, C. M. Simmons, L. E. Berkowitz, A. A. Wilber, The retrosplenial-parietal network and reference frame coordination for spatial navigation. *Behav. Neurosci.* **132**, 416–429 (2018).
22. E. L. Rounds, A. S. Alexander, D. A. Nitz, J. L. Krichmar, Conjunctive coding in an evolved spiking model of retrosplenial cortex. *Behav. Neurosci.* **132**, 430–452 (2018).
23. T. van Groen, J. M. Wyss, Connections of the retrosplenial dysgranular cortex in the rat. *J. Comp. Neurol.* **315**, 200–216 (1992).
24. B. A. Vogt, M. W. Miller, Cortical connections between rat cingulate cortex and visual, motor, and postsubicular cortices. *J. Comp. Neurol.* **216**, 192–210 (1983).
25. J. M. Wyss, T. Van Groen, Connections between the retrosplenial cortex and the hippocampal formation in the rat: A review. *Hippocampus* **2**, 1–11 (1992).
26. A. S. Alexander, D. A. Nitz, Spatially periodic activation patterns of retrosplenial cortex encode route sub-spaces and distance traveled. *Curr. Biol.* **27**, 1551–1560 (2017).
27. A. S. Alexander, D. A. Nitz, Retrosplenial cortex maps the conjunction of internal and external spaces. *Nat. Neurosci.* **18**, 1143–1151 (2015).
28. D. Mao, S. Kandler, B. L. McNaughton, V. Bonin, Sparse orthogonal population representation of spatial context in the retrosplenial cortex. *Nat. Commun.* **8**, 243 (2017).
29. A. M. P. Miller, W. Mau, D. M. Smith, Retrosplenial cortical representations of space and future goal locations develop with learning. *Curr. Biol.* **29**, 2083–2090.e4 (2019).
30. D. M. Smith, J. Barredo, S. J. Y. Mizumori, Complimentary roles of the hippocampus and retrosplenial cortex in behavioral context discrimination. *Hippocampus* **22**, 1121–1133 (2012).
31. A. Pouget, T. J. Sejnowski, Spatial transformations in the parietal cortex using basis functions. *J. Cogn. Neurosci.* **9**, 222–237 (1997).
32. L. L. Chen, L.-H. Lin, C. A. Barnes, B. L. McNaughton, Head-direction cells in the rat posterior cortex. II. Contributions of visual and ideothetic information to the directional firing. *Exp. Brain Res.* **101**, 24–34 (1994).
33. P.-Y. Jacob, G. Casali, L. Spieser, H. Page, D. Overington, K. Jeffery, An independent, landmark-dominated head-direction signal in dysgranular retrosplenial cortex. *Nat. Neurosci.* **20**, 173–175 (2017).
34. A. S. Alexander, L. M. Rangel, D. Tingley, D. A. Nitz, Neurophysiological signatures of temporal coordination between retrosplenial cortex and the hippocampal formation. *Behav. Neurosci.* **132**, 453–468 (2018).
35. J. G. G. Borst, L.-W. S. Leung, D. F. MacFabe, Electrical activity of the cingulate cortex. II. Cholinergic modulation. *Brain Res.* **407**, 81–93 (1987).
36. R. U. Muller, J. L. Kubie, The effects of changes in the environment on the spatial firing of hippocampal complex-spike cells. *J. Neurosci.* **7**, 1951–1968 (1987).
37. J. O'Keefe, N. Burgess, Geometric determinants of the place fields of hippocampal neurons. *Nature* **381**, 425–428 (1996).
38. A. T. Keinath, J. B. Julian, R. A. Epstein, I. A. Muzzio, Environmental geometry aligns the hippocampal map during spatial reorientation. *Curr. Biol.* **27**, 309–317 (2017).
39. N. R. Kinsky, D. W. Sullivan, W. Mau, M. E. Hasselmo, H. B. Eichenbaum, Hippocampal place fields maintain a coherent and flexible map across long timescales. *Curr. Biol.* **28**, 3578–3588 (2018).
40. J. Krupic, M. Bauza, S. Burton, C. Barry, J. O'Keefe, Grid cell symmetry is shaped by environmental geometry. *Nature* **518**, 232–235 (2015).
41. T. Solstad, C. N. Boccara, E. Kropff, M.-B. Moser, E. I. Moser, Representation of geometric borders in the entorhinal cortex. *Science* **322**, 1865–1868 (2008).
42. G. W. Diehl, O. J. Hon, S. Leutgeb, J. K. Leutgeb, Grid and nongrid cells in medial entorhinal cortex represent spatial location and environmental features with complementary coding schemes. *Neuron* **94**, 83–92.e6 (2017).
43. T. Hartley, N. Burgess, C. Lever, F. Cacucci, J. O'Keefe, Modeling place fields in terms of the cortical inputs to the hippocampus. *Hippocampus* **10**, 369–379 (2000).
44. C. Lever, S. Burton, A. Jeewajee, J. O'Keefe, N. Burgess, Boundary Vector Cells in the Subiculum of the Hippocampal Formation. *J. Neurosci.* **29**, 9771–9777 (2009).
45. J. M. Olson, K. Tongprasearth, D. A. Nitz, Subiculum neurons map the current axis of travel. *Nat. Neurosci.* **20**, 170–172 (2017).
46. S. D. Vann, J. P. Aggleton, E. A. Maguire, What does the retrosplenial cortex do? *Nat. Rev. Neurosci.* **10**, 792–802 (2009).
47. M. Fyhn, T. Hafting, A. Treves, M.-B. Moser, E. I. Moser, Hippocampal remapping and grid realignment in entorhinal cortex. *Nature* **446**, 190–194 (2007).
48. D. Yoganarasimha, X. Yu, J. J. Knierim, Head direction cell representations maintain internal coherence during conflicting proximal and distal cue rotations: Comparison with hippocampal place cells. *J. Neurosci.* **26**, 622–631 (2006).
49. C. Barry, R. Hayman, N. Burgess, K. J. Jeffery, Experience-dependent rescaling of entorhinal grids. *Nat. Neurosci.* **10**, 682–684 (2007).
50. D. A. Nitz, Tracking route progression in the posterior parietal cortex. *Neuron* **49**, 747–756 (2006).
51. D. A. Nitz, Spaces within spaces: Rat parietal cortex neurons register position across three reference frames. *Nat. Neurosci.* **15**, 1365–1367 (2012).

52. E. R. Chrastil, K. R. Sherrill, M. E. Hasselmo, C. E. Stern, There and back again: Hippocampus and retrosplenial cortex track homing distance during human path integration. *J. Neurosci.* **35**, 15442–15452 (2015).
53. R. A. Epstein, J. S. Higgins, K. Jablonski, A. M. Feiler, Visual scene processing in familiar and unfamiliar environments. *J. Neurophysiol.* **97**, 3670–3683 (2007).
54. S. A. Marchette, L. K. Vass, J. Ryan, R. A. Epstein, Anchoring the neural compass: Coding of local spatial reference frames in human medial parietal lobe. *Nat. Neurosci.* **17**, 1598–1606 (2014).
55. E. Z. Patai, A.-H. Javadi, J. D. Ozubko, A. O'Callaghan, S. Ji, J. Robin, C. Grady, G. Winocur, R. S. Rosenbaum, M. Moscovitch, H. J. Spiers, Hippocampal and retrosplenial goal distance coding after long-term consolidation of a real-world environment. *Cereb. Cortex* **29**, 2748–2758 (2019).
56. M. P. Brandon, A. R. Bogaard, C. P. Libby, M. A. Connerney, K. Gupta, M. E. Hasselmo, Reduction of theta rhythm dissociates grid cell spatial periodicity from directional tuning. *Science* **332**, 595–599 (2011).

Acknowledgments: We would like to thank M. Campbell, P. Castro-Mendoza, J. Dreher, E. Johansson, J. Lee, and P. Rodriguez-Echemendia for technical assistance. We also thank J. Olson and D. Nitz for useful discussions and comments pertaining to the manuscript. **Funding:** This research was supported by NIH NINDS F32 NS101836-01, NIMH R01 MH061492, MH060013, and MH120073; Office of Naval Research MURI grant N00014-16-1-2832; Office of Naval Research MURI N00014-19-1-2571; and Office of Naval Research DURIP N00014-17-1-2304. **Author contributions:** A.S.A., L.C.C., J.R.H., and M.E.H. designed the study. A.S.A. and L.C.C. conducted all experiments. A.S.A., F.R., and G.W.C. analyzed the data. A.S.A. and M.E.H. wrote the paper. All authors assisted with revision of the manuscript**. Competing interests:** The authors declare that they have no competing interests. **Data and materials availability:** All data needed to evaluate the conclusions in the paper are present in the paper and/or the Supplementary Materials. Additional data related to this paper may be requested from the authors.

Submitted 22 August 2019
Accepted 27 November 2019
Published 21 February 2020
10.1126/sciadv.aaz2322

Citation: A. S. Alexander, L. C. Carstensen, J. R. Hinman, F. Raudies, G. W. Chapman, M. E. Hasselmo, Egocentric boundary vector tuning of the retrosplenial cortex. *Sci. Adv.* **6**, eaaz2322 (2020).

Science Advances

Egocentric boundary vector tuning of the retrosplenial cortex

Andrew S. Alexander, Lucas C. Carstensen, James R. Hinman, Florian Raudies, G. William Chapman and Michael E. Hasselmo

Sci Adv **6** (8), eaaz2322.
DOI: 10.1126/sciadv.aaz2322

Science Advances (ISSN 2375-2548) is published by the American Association for the Advancement of Science, 1200 New York Avenue NW, Washington, DC 20005. The title *Science Advances* is a registered trademark of AAAS.